Stability of β nano-phases in Al-Mg-Si(-Cu) alloy under high dose ion irradiation

Camille Flament, Joël Ribis, Jérôme Garnier, Yves Serruys, F. Leprêtre, Aurélie Gentils, C. Baumier, M. Descoins, Dominique Mangelinck, A. Lopez, et al.

Accepted Manuscript

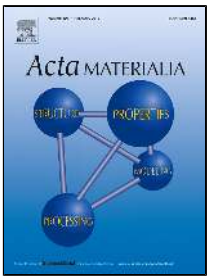

Stability of β'' nano-phases in Al-Mg-Si(-Cu) alloy under high dose ion irradiation

Camille Flament, Joël Ribis, Jérôme Garnier, Y. Serruys, F. Leprêtre, A. Gentils, C. Baumier, M. Descoins, D. Mangelinck, A. Lopez, K. Colas, K. Buchanan, P. Donnadieu, Alexis Deschamps

PII:	S1359-6454(17)30056-3
DOI:	10.1016/j.actamat.2017.01.044
Reference:	AM 13506
To appear in:	*Acta Materialia*
Received Date:	27 July 2016
Accepted Date:	22 January 2017

Please cite this article as: Camille Flament, Joël Ribis, Jérôme Garnier, Y. Serruys, F. Leprêtre, A. Gentils, C. Baumier, M. Descoins, D. Mangelinck, A. Lopez, K. Colas, K. Buchanan, P. Donnadieu, Alexis Deschamps, Stability of β'' nano-phases in Al-Mg-Si(-Cu) alloy under high dose ion irradiation, *Acta Materialia* (2017), doi: 10.1016/j.actamat.2017.01.044

Stability of β'' nano-phases in Al-Mg-Si(-Cu) alloy under high dose ion irradiation

Corresponding author: Camille Flament[1]

[1] DEN-Service de Recherches de Métallurgie Physique, CEA, Université Paris-Saclay, F-91191, Gif-sur-Yvette, France, tel : (33) 1 69 08 25 49, e-mail: camille.flament@cea.fr.

Co-authors: Joël Ribis[2], Jérôme Garnier[2], Y. Serruys[3], F. Leprêtre[3], A. Gentils[4], C. Baumier[4], M. Descoins[5], D. Mangelinck[5], A. Lopez[6], K. Colas[6], K. Buchanan[2], P. Donnadieu[7,8], Alexis Deschamps[7,8]

[2] DEN-Service de Recherches Métallurgiques Appliquées, CEA, Université Paris-Saclay, F-91191 Gif sur Yvette, France
[3] DEN-Service de Recherches de Métallurgie Physique, Laboratoire JANNUS, CEA, Université Paris-Saclay, F-91191, Gif-sur-Yvette, France
[4] CSNSM, Univ Paris-Sud, CNRS/IN2P3, Université Paris Saclay, 91405 Orsay, France
[5] IM2NP, Aix-Marseille Univ & CNRS, 13397 Marseille, France
[6] DEN-Service d'Etude des Matériaux Irradiés, CEA, Université Paris-Saclay, F-91191 Gif sur Yvette, France
[7] Université Grenoble Alpes, SIMAP, F-38000 Grenoble, France
[8] CNRS, SIMAP, F-38000 Grenoble, France

Stability of β'' nano-phases in Al-Mg-Si(-Cu) alloy under high dose ion irradiation

Camille Flament[1*], Joël Ribis[2], Jérôme Garnier[2], Y. Serruys[3], F. Leprêtre[3], A. Gentils[4], C. Baumier[4], M. Descoins[5], D. Mangelinck[5], A. Lopez[6], K. Colas[6], K. Buchanan[2], P. Donnadieu[7,8], Alexis Deschamps[7,8]

[1] *DEN-Service de Recherches de Métallurgie Physique, CEA, Université Paris-Saclay, F-91191, Gif-sur-Yvette, France*

[2] *DEN-Service de Recherches Métallurgiques Appliquées, CEA, Université Paris-Saclay, F-91191 Gif sur Yvette, France*

[3] *DEN-Service de Recherches de Métallurgie Physique, Laboratoire JANNUS, CEA, Université Paris-Saclay, F-91191, Gif-sur-Yvette, France*

[4] *CSNSM, Univ Paris-Sud, CNRS/IN2P3, Université Paris Saclay, 91405 Orsay, France*

[5] *IM2NP, Aix-Marseille Univ & CNRS, 13397 Marseille, France*

[6] *DEN-Service d'Etude des Matériaux Irradiés, CEA, Université Paris-Saclay, F-91191 Gif sur Yvette, France*

[7] *Université Grenoble Alpes, SIMAP, F-38000 Grenoble, France*

[8] *CNRS, SIMAP, F-38000 Grenoble, France*

Abstract

The microstructure of a 6061-T6 Al alloy subjected to ion irradiation at 95 and 165 displacements per atom (dpa) has been evaluated by transmission electron microscopy and atom-probe tomography. The initial microstructure of the alloy is dominated by needle-shaped β'' precipitates. After 95 dpa irradiation, the β'' precipitates display a slight lattice distortion and are partially dissolved, together with the formation of a new phase. After 165 dpa irradiation, the β'' precipitates are completely dissolved, the new phase has grown and a high density of clusters rich in Mg, Si, Cu and Cr is observed. The determination of ballistic versus radiation enhanced diffusion coefficients shows that enhanced diffusion is predominant for β" dissolution. The formation and growth of the new particles may be caused by radiation induced segregation. Solute drag by vacancies or mixed dumbbell interstitials migration could explain the diffusion of some elements as Si or Cr towards the new particles.

Keywords: aluminium alloys, β'' nano-phases, irradiation effect, transmission electron microscopy, atom-probe tomography.

*Corresponding author. Tel.: +33 1 69 08 25 49; fax: +33 1 69 08 68 67. E-mail address: camille.flament@cea.fr (C. Flament).

1. Introduction

Due to their specific strength, high corrosion resistance and welding performance, aluminum alloys are widely used as structural parts. In addition, their low capture cross section of fast and thermal neutrons makes them suitable for use in water-cooled research reactors. Because of thermally induced precipitation which provides a good compromise of mechanical properties (ductility and fracture toughness), 6000 series Al-Mg-Si alloys are preferred to 5000 series Al-Mg alloys for internal structures of research reactors such as the core vessel of the new European materials testing reactor Jules Horowitz [1]. The high strength of Al-Mg-Si alloys is due to the precipitation of nano-scaled phases β'' during a T6 heat treatment at ~170°C. More generally, the Al-Mg-Si alloy family decomposes from the supersaturated solid solution according to the following sequence:

Supersaturated solid solution → atomic clusters → GP zones → β'' → β',U1,U2,B' → β [2–5]

β'' are metastable needles along the $<100>_{Al}$ axes and semi-coherent with the matrix [2]. Analyses by small angle neutron scattering (SANS) associated with transmission electron microscopy (TEM) observations show that their typical length is less than 50 nm with a diameter around 4 nm [6]. Using high resolution transmission electron microscopy (HRTEM) and structural refinements, Zandbergen et al. [7] identified their crystallographic structure as being C-centered monoclinic with the lattice parameters a=1.516 nm, b= 0.405 nm, c= 0.674 nm and β=105.3°. Edwards et al. [8] and Matsuda et al. [9] determined the structure to be monoclinic as well albeit with different values of lattice parameters.

The stoichiometry of β'' is generally set as being Mg_5Si_6 [2,7,10] in Al-Mg-Si alloys with excess Si whereas Murayama et al. [11] and Maruyama et al. [12] demonstrated that their Mg : Si atomic ratio approaches 1.7 in a balanced alloy (Al-Mg_2Si stoichiometry). More recent articles based on atom-probe tomography (APT) [13,14] have shown that β'' can contain Al

atoms leading to the stoichiometry $Mg_5Al_2Si_4$ which is the most energetically favorable chemistry determined by density functional theory (DFT) [14,15]. Moreover with the addition of more than 0.1 wt% of Cu to the alloys, the sequence of precipitation written above can be modified [16–20]. A Cu- rich lath shaped phase called L can precipitate in the same range of temperatures as β'' [17,20–23]. Based on the difference of morphology and contrast between these two precipitate families, it has been estimated that the L phase represents ~20% of the total number in a balanced alloy with 0.28 wt% of Cu [24].

The precipitation sequence expresses that β'' disappears in favor of the metastable β' rod-shaped phase above a temperature of about 200°C [3,25]. β' is larger (typically 10 nm in diameter and between 100 and 500 nm in length) than β'' and displays a different crystallographic structure, namely hexagonal [3]. The mechanism of the β''- β' transformation is not well known yet. *In situ* small angle X-ray scattering (SAXS) investigations by Tsao et al. [26] suggested that β' phases precipitation occurred along the dissolution of β'' when the temperature was increased to 260°C.

Although un-irradiated Al-Mg-Si alloys have been widely studied, only few articles investigate their microstructural evolutions under irradiation, which is of major concern when evaluating the evolution of mechanical properties in such reactor conditions. Farrell et al. [27] studied the microstructure of 6061-T6 alloy used in a nuclear reactor. Based on the study of selected area electron diffraction patterns they suggested that β'' type precipitates are still present after neutron irradiation at a fast neutron flux of $1.3x10^{23}$ $n_{fast}.cm^{-2}$. Nevertheless, no information exists on their believed change of shape, size, structure and chemistry due to irradiation. According to Weeks et al. [28], β'' are dissolved by a flux of $2x10^{22}$ $n_{fast}.cm^{-2}$ neutron irradiation since the diffraction streaks corresponding to β'' are observed to disappear. They observed spherical particles after irradiation, believed to be pure Si and potentially amorphous particles, resulting from the Al transmutation into Si by the thermal neutron flux [27–29]. This apparent

discrepancy about β'' evolution under neutron irradiation can be due to misinterpretation of TEM images whose contrast is complicated by the presence of irradiation defects and transmutation products. It is then necessary to associate TEM observations with other nano-characterization techniques.

In order to bring additional information on β'' evolution under irradiation, this paper presents detailed transmission electron microscopy (TEM) and atom-probe tomography (APT) studies of the stability of β'' precipitates under controlled ion irradiation at room temperature at different doses.

2. Experimental procedure

2.1. Material

The investigated material is the 6061-T6 Al alloy with the chemical composition given in Table 1. It comes from a full-scale vessel demonstrator. The cast alloy was first homogenized at 530°C for 6 hrs followed by several stages of hot forging at 460°C and one stage of backward extrusion. It was then solution treated at 530°C for 3 hrs followed by a water quench and an axial compression of 3%. Then, the alloy was aged at 170°C for 8 hrs.

Element	Si	Mg	Fe	Cr	Cu	Mn	Zn	Ti
wt.%	0.58	1.00	0.16	0.19	0.28	0.06	0.03	0.02

Table 1. Chemical composition (wt. %) of the 6061-T6 aluminum alloy

2.2. TEM

After mechanical polishing of thin sheets, discs of 3 mm in diameter were punched out and electro-polished in a double jet Struers Tenupol device. The electrolyte was a mixture of ethanol, 2-butoxyethanol, perchloric acid and water. The thinning was performed at 30V at 0°C followed by a PIPS (Precision Ion Polishing System) cleaning (3keV at angles of 4° on both side of the foil).

TEM 200 kV JEOL 2100 (LaB_6 filament) and 300 kV JEOL 3010 (LaB_6 filament) instruments were used for Bright Field (BF) and Dark Field (DF) observations as well as selected area electron diffraction (SAED) patterns acquisitions. The crystallographic structure of pre- and post-irradiated precipitates was investigated by high resolution TEM (HRTEM) in a 200 kV FEG-JEOL 2010 instrument.

TEM samples of 6061-T6 alloy were thermally annealed *in situ* in the 200 kV FEI Tecnai of the CSNSM TEM at the JANNuS Orsay facility [30]. This instrument is equipped with a double tilt heating sample holder. The temperature was first raised to 180°C for 5 min. From 180°C, the sample was isothermally held 5 min every 10°C with a heating rate between these stages of 1°C/min, up to a final temperature of 290°C.

The *in situ* ion irradiation was performed at the JANNuS-Orsay facility at the CSNSM [30, 31], which is equipped with the 200 kV Tecnai TEM coupled with two ion accelerators (only the 2 MV ARAMIS ion accelerator was used in this study). A thin foil of 6061-T6 alloy previously cleaned in a double jet Ar/H_2 plasma cleaner for 2 min was irradiated with 4 MeV Au^{2+} ions at room temperature. The specimen was tilted such that the β'' precipitates could be observed in dark field imaging in the $[110]_{Al}$ zone axis. The ion beam line made a 27º angle with the normal of the specimen surface. The total fluence reached was measured to be $2.1x10^{16}$ $Au^{2+}.cm^{-2}$ for a flux of $2x10^{11}$ $Au^{2+}.cm^{-2}.s^{-1}$, corresponding to an irradiation time of 29 hrs. In parallel, an *ex situ* 2 MeV W^{3+} ion irradiation of a thin foil of 6061-T6 was performed at room temperature at the JANNuS-Saclay irradiation facility on the Épiméthée accelerator [32]. The angle between the beam line and the sample surface was 15°. The thin foil was irradiated at a fluence of $2.9x10^{16}$ $W^{3+}.cm^{-2}$ at a flux of $3.1x10^{11}$ $W^{3+}.cm^{-2}.s^{-1}$, corresponding to a total irradiation time of 26 hrs.

The depth profiles of the displacement damage (Figure 1) were estimated using the Kinchin Pease method of the SRIM-2013 code [33,34] with a displacement threshold energy for

aluminium atoms of 16 eV [35,36]. The maximum doses reached within 150 nm (the mean thickness of the thinned zone of the foil) for the *in situ* and *ex situ* irradiations were estimated to be respectively 95 and 165 dpa (displacements per atom). The influence of Au and W implantation was considered to be negligible at this given depth as observed on the SRIM concentration profile of Figure 1.

2.3. APT

Chemical characterization was performed by atom-probe tomography (APT) at CEA/SEMI (Saclay, France) for un-irradiated materials and at IM2NP (Marseille, France) for irradiated materials. APT specimens were prepared from un-irradiated and irradiated thin foils using a FEI Focused Ion Beam microscope. APT analysis of un-irradiated materials was performed on a CAMECA LEAP 4000XHR instrument operating in laser mode with an energy of 40 pJ per pulse (laser wavelength of 355 nm) at a repetition rate of 250 kHz. The irradiated samples were analyzed in a CAMECA LEAP 3000XHR instrument operating at 40 pJ per pulse (laser wavelength of 532 nm) at repetition rate of 250 kHz. For both analyses, the temperature of the specimen was maintained at 40 K. APT data were reconstructed using the software IVAS 3.6.6 from CAMECA. The compression factor and the k factor used for reconstructions were respectively 1.4 and 4.4 for un-irradiated samples and 1.6 and 4.55 for irradiated samples. They were chosen based on the identification of the poles <200> and <220> respectively in order to get the right value of inter-reticular plane distances along the z axis. The "nearest neighbour distribution" method was used in order to identify the precipitates chemistry [37]. Several parameters are defined such as d_{max} which corresponds to the maximum distance between two solutes in one cluster. The second parameter is N_{min} which corresponds to the minimum number of solute atoms that constitutes a significant cluster. Below N_{min} potential clusters are considered as random fluctuations. The erosion parameter d_{er} which removes atoms around the cluster interface with the matrix and the "envelope parameter" L which takes into account

matrix atoms that should be denoted as being contained in the cluster [37]. These four parameters chosen for the cluster identification of the un-irradiated and irradiated sample are reported in Table 2.

	d_{max}	N_{min}	d_{er}	L
Un-irradiated material	0.6	50	0.6	0.6
Irradiated material (same as in [38])	0.6	20	0.6	0.6

Table 2. Chosen parameters for clusters identification.

3. Results

3.1. Characterization of un-irradiated β'' precipitates

Figure 2.a is a selected area electron diffraction (SAED) pattern along the $[100]_{Al}$ zone axis. The diffuse streaks observed at the (100) forbidden reflections of the Al matrix (schematized in orange and indicated by an arrow on the diffraction pattern) correspond to the needle-shaped β''-type precipitates in the reciprocal lattice. Figure 2b shows a dark field (DF) micrograph obtained by selecting these streaks with a contrast aperture, showing β''-type precipitates along $<100>_{Al}$ directions, where the contrast related to the matrix deformation around the semi-coherent nano-phases is suppressed [39]. The average radius of the needles $r_{\beta''}$ measured from DF images along $[100]_{Al}$ is 2.5 ± 0.5 nm and their average length $L_{\beta''}$ is 36.5 ± 0.5 nm. The number density of precipitates estimated on bright field TEM images is (4.0 ± 0.5) x 10^{22} m^{-3} considering a thickness of 80 nm determined by electron energy loss spectrometry (EELS).

The crystallographic structure of these β'' precipitates was investigated by HRTEM. Figure 3.a is an example of a β''-type needle oriented along the electron beam direction while Figure 3.b is a filtered view of Figure 3.a. The Fast Fourier Transformed image of Figure 3.a presented on Figure 3.c is compared to simulated diffraction patterns (Figure 3.d) and data from literature [2,8]. It indicates that the inter-reticular distances and angles correspond to (001), (200), (201) and (20-1) atomic planes with d_{001} = 0.65 ± 0.02 nm, d_{200} = 0.75 ± 0.03 nm, d_{201} = 0.46 ± 0.02

nm, $d_{20\text{-}1}$ = 0.57 ± 0.02 nm and 33 ± 3 ° between (001) and (201), 40 ± 5 ° between (201) and (200), 63 ± 5 ° between (200) and (20-1). This is consistent with a centered monoclinic structure oriented along the [010] zone axis with lattice parameters close to a = 1.52 nm, c = 0.67 nm and β = 105 ° determined by Andersen et al. [2] (at ± 0.02 nm and 5°). To estimate the parameter 'b', one β'' precipitate has been observed with its 'b' axis perpendicular to the electron beam as shown in Figure 4.a. The same analysis as previously indicates that it corresponds to (510) and (020) atomic planes. This is also consistent with a centered monoclinic structure oriented along the [001] zone axis with the same a, c and β parameters as previously and with b = 0.41 nm. The filtered image in Figure 3.b shows that the [100] axis of β'' is parallel to [032] axis of the matrix as well as $[001]_{\beta''}$ is parallel to $[01\text{-}3]_{Al}$. As the precipitate oriented along the [010] zone axis is surrounded by a matrix oriented along the [100] zone axis, the orientation relationship of this nano-precipitate with the matrix is $(100)_{Al}$ // $(010)_{\beta''}$; $[01\text{-}3]_{Al}$ // $[001]_{\beta''}$; $[032]_{Al}$ // $[100]_{\beta''}$. This orientation relationship is one of the 12 variants of the orientation $(010)_{\beta''}$ // $\{100\}_{Al}$; $[001]_{\beta''}$ // $<310>_{Al}$; $[100]_{\beta''}$ // $<230>_{Al}$ determined by Yang et al. [40]. It is worth noting that no misfit dislocation has been observed at the β''/Al interface as expected regarding the localized coherency of the interfaces (expected to be coherent with the matrix along their 'b' axis) [2,8].

The chemistry of the nano-precipitates was evaluated by APT analyses. Figure 5 shows the distribution of Mg, Si and Cu atoms in a reconstructed tip. Mg, Si and Cu are preferentially located in needles oriented along three perpendicular directions. Three spheroidal clusters containing Mg and Si are also observed. They could be consistent with GP zones/solute clusters remaining after T6 heat treatment [11].

The amount of Mg, Si, Cu and Al was investigated using the method described in section 2.3. For the 8 precipitates studied, the Mg : Si ratio ranged between 1.5 and 2.2 and the Mg : Cu ratio ranged between 6.5 and 12.5. The average Al content of the precipitates was 48.8 ± 0.5

at%. This value may be overestimated, since the evaporation field of the precipitates is higher than that of the matrix which is likely due to the strong covalent Si-Si bond in β'' precipitates [41]. This induces trajectory aberrations and overlap of elements from the matrix and from the precipitate at the matrix/precipitate interface.

3.2. Characterization after *in situ* thermal annealing

The evolution of β'' needle-shaped nano-precipitates has been followed *in situ* during heating following the procedure described in section 2.2, as a reference evolution when diffusion of solute is thermally activated. The zone of interest is oriented along an $[100]_{Al}$ zone axis. The precipitates observed in BF at different temperatures were all elongated along this axis as shown in Figure 6, so that the equivalent radius of their cross-section could be measured. The radius distributions of the precipitates for the temperatures 200, 240 and 270°C are reported on the histograms of Figure 7. Between 200 and 240°C, the radius distribution of precipitates is almost stable, with an average value decreasing from 2.4 to 2.2 nm. The number density also decreases from $(1.7 \pm 0.5) \times 10^{22}$ .m^{-3} to $(9.0 \pm 0.5) \times 10^{21}$ .m^{-3} for a thickness of 80 nm determined by EELS. These results suggest a partial dissolution of the β'' precipitates. When the sample is heated from 240 to 270°C, the radius distribution becomes bimodal. Part of the distribution spreads from 1.4 to 2.2 nm whereas the other part spreads from 2.6 to 6.2 nm. The smallest precipitates continue to dissolve whereas larger precipitates form. The number density decreases from $(9.0 \pm 0.5) \times 10^{21}$ .m^{-3} to $(3.2 \pm 0.5) \times 10^{21}$ .m^{-3}. From this size distribution it can be inferred that the large precipitates forming along the dissolution of the β'' precipitates are β'-type phases.

3.3. Characterization of the precipitates after irradiation

As before irradiation, DF imaging was used to image the β'' precipitates after ion irradiation. Figure 8.a shows an electron diffraction pattern of the alloy irradiated by Au^{2+} ions at room temperature to 95 dpa. The image of Figure 8.b is obtained by the selection of the diffuse streaks

corresponding to the β'' precipitates. No significant evolution of the needles is qualitatively observed. From such images the size distribution of the β'' precipitates has been measured and compared to that before irradiation. Figure 9.a and Figure 9.b are respectively the histograms of radius and length distribution of β'' before and after 95 dpa irradiation. Both histograms show a displacement towards smaller values. Before irradiation the radius ranges from 1.2 nm to 4.6 nm with a maximum number of particles having a radius of 2.6 nm. After 95 dpa irradiation the radius ranges from 1.2 nm to 4.0 nm with a maximum number of particles having a radius of 2.0 nm. The mean radius changes from 2.5 nm to 2.0 ± 0.5 nm. This also applies for their length which ranges from 10 nm to 110 nm before irradiation whereas it ranges from 10 nm to 80 nm after 95 dpa irradiation. The average value changes from 36.5 nm to 22.5 ± 0.5 nm. These results demonstrate a partial dissolution of the β'' nano-phases after 95 dpa irradiation. The number density of particles slightly decreased, from 4 to (3.5 ± 0.3) x 10^{22} $.m^{-3}$ for a sample thickness of 110 nm determined by EELS which could be related to the complete dissolution of the smallest particles.

A high resolution image of a β'' nano-precipitate after irradiation, oriented along a [100] matrix direction, is presented on Figure 10.a. The Fast Fourier Transform of Figure 10.c is compared to the simulated centered monoclinic structure oriented along [010] zone axis. It indicates that the measured inter-reticular distances and angles correspond to (001), (200), (201) and (20-1) atomic planes of the β'' structure, with d_{001} = 0.55 ± 0.01 nm, d_{200} = 0.80 ± 0.02 nm, d_{201} = 0.40 ± 0.02 nm, $d_{20\text{-}1}$ = 0.51 ± 0.01 nm and 35 ± 4 ° between (001) and (201), 44 ± 4 ° between (201) and (200), 58 ± 3 ° between (200) and (20-1). These values differ by 6% ((200) plane) up to 20% ((001) plane) from those of the non-irradiated nano-precipitate. This means that irradiation may induce a slight lattice distortion. Figure 10.b shows that $[100]_{\beta''}$ // $[02\text{-}3]_{Al}$ and $[001]_{\beta''}$ // $[0\text{-}3\text{-}1]_{Al}$ for the nano-precipitate oriented along [010] zone axis embedded in a matrix oriented along [100] zone axis. The orientation relationship of this nano-precipitate is $(100)_{Al}$ // $(010)_{\beta''}$

; $[02\text{-}3]_{Al}$ // $[100]_{\beta''}$; $[0\text{-}3\text{-}1]_{Al}$ // $[001]_{\beta''}$, which is still among the 12 variants determined by Yang et al. [40] for un-irradiated materials. Thus, despite their evolution (dissolution and possible distortion of lattice), the orientation relationship between the precipitates and the matrix is not altered after 95 dpa irradiation.

Figure 11.a represents a diffraction pattern of the 6061-T6 Al alloy along $[100]_{Al}$ zone axis irradiated at room temperature with W^{3+} ions to 165 dpa. The diffuse streaks corresponding to β'' nano-precipitates are not observed anymore. The DF image from the selection of the forbidden spots of Al is presented in Figure 11.b. No β'' needle-shaped precipitate is observed. It can therefore be concluded that the ion irradiation of 165 dpa totally dissolved the β'' precipitates.

The alloy has also been observed by DF imaging along a $[112]_{Al}$ zone axis, both before irradiation and after 95 dpa and 165 dpa irradiations. The DF images of Figure 12 were obtained according to the diffraction conditions designated by a red circle on the diffraction patterns. These observations highlight the presence of a new population of nano-precipitates that appeared under ion irradiations. Their coexistence with β'' precipitates at 95 dpa indicates that they appear concurrently to β'' dissolution. The average radius of the new objects is 1.8 ± 0.5 nm after 95 dpa irradiation and 3.8 ± 0.5 nm after 165 dpa irradiation. Their number density is of the order of $(2.4 \pm 0.9) \times 10^{21}$ $.m^{-3}$ for both irradiation conditions in the same DF conditions. The microstructure of the alloy irradiated to 165 dpa has also been characterized by atom-probe tomography. An APT reconstructed volume is presented in Figure 13. Consistently with the TEM observations, no β'' needle-shaped precipitate is observed. The only features present in the tip are clusters rich in Mg, Si, Al, Cu and Cr. The Mg : Si atomic ratio is above 1 for all clusters and approaches 5 for larger clusters. Their number density is estimated by [42]:

$$N = \frac{N_p \zeta}{N_{vol} \Omega} \quad (1)$$

with N_p number of precipitates in their entirety (174 ± 10), ζ detector efficiency (37%), N_{vol} total number of detected atoms (4726622 atoms) et Ω atomic volume (1.66 x 10^{-29} m^3). The total cluster number density is approximately (8.2 ± 0.5) x 10^{23} $.m^{-3}$, which is above the one determined by TEM image analyses (2.4 x 10^{21} $.m^{-3}$) by more than two orders of magnitude. This suggests that most of the clusters observed in the APT tip are isostructural clusters which are not observed in TEM, and that only a few of these objects have a defined structure and a common direction with $[112]_{Al}$.

Figure 14.a is a high resolution TEM image of such a precipitate. The study of the associated FFT (Figure 14.b) is not sufficient to accurately determine its structure and its orientation with the matrix. Nevertheless the ratio d_1 : d_2 of 1.0 and d_1 : d_3 of 2.2, the angles between d_1 and d_2 and between d_3 and d_2 reported on Figure 14.b do not match with the centered monoclinic structure of β'' nano-precipitates but with a potential cubic structure oriented along [110] zone axis. According to their size, their chemistry (probably Mg rich from the APT observations) and their structure, one can reasonably state that these precipitates formed under irradiation do not belong to the precipitation sequence of β-type phases.

4. Discussion

4.1. β'' before irradiation

HRTEM analyses of the needle-shaped precipitates in the present Al - 1.0Mg - 0.58Si - 0.28Cu (wt%) (balanced) alloy demonstrate that they display a centered monoclinic structure with lattice parameters in agreement with Andersen et al. [2] and Edwards et al. [8] who studied excess Si alloys. The crystallographic structure as well as the orientation relationship of the precipitates with the matrix, which can be written as: $(010)_{\beta''}$ // $\{100\}_{Al}$; $[001]_{\beta''}$ // $<310>_{Al}$;

$[100]_{\beta''}$ // $<230>_{Al}$ [40], seem therefore to be independent of the alloy composition and fabrication. APT analyses show that these β'' precipitates contain Mg, Si, Cu and Al with a Mg : Si ratio close to 2. Several studies have already demonstrated that β'' nano-precipitates may contain Al and Cu [15,43]. High resolution electron dispersive X-ray spectroscopy (EDX) mapping and APT analyses performed in a 1.15 Mg, 1.14 Si et 0.268 Cu (at%) alloy by Li et al. [18] highlight that the average composition of β'' may be 28.6Al – 38.7Mg – 26.5Si – 5.17Cu (at%) with Al and Cu in substitution of the same Si3 and Mg1 columns of the monoclinic structure proposed by Andersen [2]. They found an Al content in the precipitates lower than the one determined in this study. Similarly, the assessment by Hasting et al. [14] provided an estimate of the Al content in the precipitates between 20 and 30 at% in a Cu-free alloy. This supports the likely overestimation of Al content in β'' in APT observations, caused by evaporation artefacts. As for the Mg : Si ratio, several studies tend to show that it follows the matrix composition. Murayama et al. [11] as well as Maruyama et al. [12] demonstrated by respectively 3 DAP and EDS analyses that for a balanced alloy the atomic ratio Mg : Si in β'' is 1.7. This supports the Mg : Si ratio estimated by APT for the balanced alloy analyzed in this study. A recent HAADF-STEM study combined with EDX measurements performed by Saito et al. [44] showed that in Al – 0.52Mg – 0.38Si – 0.04Cu (at%), Cu is preferentially located close to the interface β''/Al and suppresses misfit dislocations. Such a phenomenon could explain the absence of misfit dislocations noticed around the β'' nano-precipitates observed in this study.

4.2. 6061-T6 Al alloy under ion irradiation

β'' dissolution

Dark field TEM observations in $[100]_{Al}$ zone axis and APT analyses highlight that β'' nano-phases dissolve at room temperature under ion irradiation. Collision cascades created by the energetic Au^{2+} and W^{3+} ions causing atoms displacement may be responsible for this dissolution

of precipitates. However the *in situ* annealing performed at 290°C reveals that when the thermodynamic conditions are changed, β'' dissolve partially before transforming to β', since the radius and density of precipitates decrease with increasing temperature. This behavior under annealing suggests that accelerated diffusion may cause β'' precipitates dissolution under room temperature ion irradiation, provided that the irradiation flux corresponds to a thermodynamic forcing (increased effective temperature) [45,46]. To test these two hypotheses, we have calculated and compared ballistic and thermodynamic diffusion coefficients to estimate which of these mechanisms is predominantly at the origin of the dissolution of precipitates. The ballistic diffusion coefficient is determined from [45]:

$$D^b = \frac{1}{6} R\lambda^2 \quad (2)$$

where R is the defect production rate equal to 1.7 x 10^{-3} dpa.s^{-1} and λ is the average relocation distance of Mg and Si atoms due to ballistic ejection. This distance can be estimated considering the Heinig et al. model [47] which defines the spatial probability distribution $W_\infty(\delta)$ of atoms displaced from a flat interface into the neighboring half space. It is expressed as:

$$W_\infty(\delta) = \frac{q}{2}\left(1 + \frac{\delta}{2\lambda}\right)\exp\left[\frac{-\delta}{\lambda}\right] \quad (3)$$

were δ is the radial distance from the nano-precipitate surface, q a parameter depending on atomic masses, displacement energies, etc., and λ the mean displacement distance. λ can be estimated fitting the Si, Mg.ions^{-1}.nm^{-1} graph from TRIM calculations applied to a 5 nm diameter (Mg_2Si) nano-precipitate surrounded by a 10 nm thick Al matrix irradiated with W^{3+} (2MeV) ions (Figure 15). The average values of λ are 0.3 and 0.25 nm respectively for Si and Mg atoms (average of backward and forward atoms displacements values). Thus the ballistic

coefficient is estimated to be ~2.5 x 10^{-19} $cm^2.s^{-1}$ for Si atoms and ~1.8 x 10^{-19} $cm^2.s^{-1}$ for Mg atoms.

The radiation-enhanced diffusion coefficient is determined from the vacancy diffusion coefficient which is expressed as [48]:

$$D_v = \alpha a^2 \upsilon \exp\left(\frac{-E_m^v}{k_B T}\right) \quad (4)$$

T is the temperature of irradiation, k_B the Boltzman constant, α a geometric factor close to 1, a the lattice parameter of Al equal to 0.405 nm and υ the Debye frequency. For a vacancy migration energy E_m^v in pure Al equal to 0.52 eV [49], the vacancy diffusion coefficient in Al at room temperature is calculated to be : 2.6 x 10^{-11} $cm^2.s^{-1}$. From this coefficient, the time for vacancies to reach sinks τ can be calculated by the following formula [48]:

$$\tau = \frac{1}{D_v k^2} \quad (5)$$

where k^2 is the sink strength. In the 6061-T6 Al alloys the main point defect sinks are the needle shaped β'' precipitates present in high density. We neglect the influence of grain boundaries and incoherent dispersoids, which are present in low density compared to β''. β'' phases are coherent with the matrix along their <010> axis. Assuming that the needles act as perfect defects traps, the sink strength of a precipitate of arbitrary shape is expressed as [50]:

$$k^2 = \frac{4\pi\phi\kappa}{v_p} \quad (6)$$

where ϕ is the volume fraction of precipitates, v_p the volume of a precipitate and κ the electrical capacitance of an isolated metal electrode of the same size as the precipitate. In first approximation Brailsford et al. [50] indicate that for many cases (lenticular discs, prolate

ellipsoids) κ can be approximated at 0.3 $A^{1/2}$ with A the surface area. Using this first approximation and considering β'' precipitates as cylinders with an area of $2\pi r_{\beta''} L_{\beta''}$ and a volume fraction of $v_p N$ with N the density of precipitates (4 x 10^{22} $.m^{-3}$), the sink strength is estimated to be 3.6 x 10^{11} cm^{-2}. Thus the time for vacancies to reach the sink is 0.1 s. This value is low compared to the duration of the irradiation (~10^5 s), which indicates that the non-equilibrium concentration of vacancies is not controlled by the recombination regime, but by the sink density. In the sink annihilation regime the concentration of non-equilibrium vacancies is calculated by [48]:

$$C_v^{irr} = R\tau \quad (7)$$

It is equal to 1.7 x 10^{-4} vacancies. In these conditions the radiation-enhanced diffusion coefficient D^{irr} can be determined by the formula [48]:

$$D^{irr} = \frac{C_v^{irr}}{C_v^{eq}} D^{th} = R\tau \exp\left(\frac{E_f^v}{k_B T}\right) D^{th} \quad (8)$$

where C_v^{eq} is the equilibrium vacancy concentration, E_f^v the vacancy formation energy in pure Al equal to 0.69 eV [51] and D^{th} the thermal diffusion coefficient. We estimate D^{th} for Mg and Si, the main alloying elements which control β'' nano-precipitates formation [8], using the Arrhenius equation :

$$D^{th} = D_0 \exp\left(-\frac{Q}{RT}\right) \quad (9)$$

The values of pre-exponential factor D_0 and activation energy Q reported in Table 3 have been determined by Du et al. [52]. The thermal diffusion coefficients of Mg and Si at 25°C are respectively equal to 1.1 x 10^{-22} and 3.3 x 10^{-22} $cm^2.s^{-1}$. The diffusion coefficient under

irradiation D^{irr} at room temperature of Mg is 9 x 10^{-15} $cm^2.s^{-1}$ and is equal to 2.6 x 10^{-14} $cm^2.s^{-1}$ for Si. The radiation-enhanced diffusion coefficient is 10^5 times higher than D^b. In absence of irradiation effects, a coefficient D^{th} equal to 10^{-15} $cm^2.s^{-1}$ leads to an effective temperature T^{eff} of 172°C which is below the expected temperature of β'' dissolution during annealing (>200°C) except that irradiation at this effective temperature lasts a long time being 26 hrs. Thus it seems that radiation-enhanced diffusion is predominant for β'' dissolution as compared to ballistic mixing.

Diffuser	D_0 (cm^2/s)	Q (kJ/mol)
Mg	1.49x10^{-1}	120.5
Si	1.38x10^{-1}	117.6

Table 3. Calculated Arrhenius parameters for diffusion coefficients of Mg and Si in fcc Al [52].

Formation of new particles

During high temperature annealing, coarser needles along $<100>_{Al}$ appear while β'' ones dissolve as predicted by the precipitation sequence. Such needles are not observed after ion irradiations but rather a high density of clusters appear, containing Mg, Si, Al, Cu and Cr, a few having a well-defined structure and a size similar to the radius of the β'' precipitates. These precipitates cannot belong to the β precipitation sequence because of their non C centered monoclinic structure, their orientation with the matrix, and their chemistry, especially the presence of Cr, which was not part of β'' initially. Therefore, the presence of these particles is directly caused by irradiation. β'' dissolution by accelerated diffusion and ballistic mixing to a lesser extent actually brings Mg, Si and Cu atoms in solid solution. This results in a strong driving force for precipitation of Mg and Si. During 6061-T6 fabrication, the supersaturation in solutes and vacancies after solutionizing and quench leads to the formation of separate Mg- and Si-rich clusters followed by the formation of (Mg,Si)- and vacancy-rich co-clusters [8]. These clusters are fully coherent with the matrix. During ion irradiation, change of precipitation

kinetics and supersaturation of vacancies and solutes in solid solution may also induce the formation of Mg, Si and potentially vacancy rich clusters (VRC). Such VRCs, likely coherent with the matrix could act as defect sinks and grow by radiation induced segregation (RIS). RIS has been observed at grain boundaries after 165 dpa ion irradiation as shown on EDX maps of Mg and Si atoms in Figure 16 (performed on JEOL 2010 in Scanning TEM (STEM) mode). Solute drag by vacancies could be responsible for solute diffusion towards sinks during irradiation. Several first principles calculations [53,54] of solute-vacancy binding energies in Al show that Si-vacancy binding is attractive since it is largely positive at about 0.08 eV (NN vacancy binding) [53]. Several authors determined that Si is dragged by vacancies at temperatures below 600K [55] (five-frequency model). A similar assessment stands for Cu, which has a slightly positive binding energy (about 0.02-0.04 eV [53]) and can be driven by vacancies at temperatures below 1300K [55]. Vacancy binding does not seem to fit for Mg and Cr. Indeed Mg binding energy is -0.02 eV and is equal to -0.25 eV for Cr [53]. Concerning Cr, its presence in the particles is not expected since it does not belong to β'' nano-precipitates initially. Before irradiation, Cr is entirely precipitated in Al(Cr,Fe,Mn)Si dispersoids. The dispersoids display a core/shell organization with Cr in shell and (Mn,Fe) in core which is enhanced by electron irradiation [56]. After ion irradiation, Cr close to the dispersoid/matrix interface is likely to be driven into solution by ballistic mixing as seen in the Cr APT map (Figure 13). DFT calculations performed by Klaver et al. [57] show that the (100) dumbbell configuration for Al-Cr is stable. The diffusion of such complexes could be responsible for the presence of Cr in the clusters. This configuration is not stable for Mg atoms and it cannot be dragged by vacancies at room temperature [54,55]. The segregation of Mg towards sinks in Al is not well understood yet.

The observation of new particles in Al-Mg-Si alloys after ion irradiation echoes the study of Ueyama et al. [58] who observed Mg, Si rich clusters by APT analyses after 16 MeV Au^{5+}

irradiation of an Al-Mg-Si solid solution. Mitsuda et al. [38] also observed clusters containing Mg, Si and Cu in Al-Mg-Si-Cu solid solution irradiated using I^{3+} ions. Both teams have performed Vickers hardness tests at room temperature on irradiated Al-Mg-Si(-Cu) solid solution for different irradiation times and compared to the un-irradiated solid solution for different times of ageing at 453K (needed for β'' formation). They showed that the peak hardness of irradiated alloy reached while clusters form is higher than the one of aged alloy reached as β'' precipitates. Thus it seems that irradiation induced clusters have a higher hardening effect than β'' precipitates, although one must remain careful due to the possible contribution of other irradiation defects such as dislocation loops. Up to our knowledge the precipitation of particles containing Cr in an ion irradiated T6 Al-Mg-Si alloy following the dissolution of needle-shaped β'' type precipitates has not been observed before. Although they are smaller and in higher density than β'', the newly formed clusters may have a positive impact on the hardness of the alloy as observed by Ueyama et al. [58]. Weeks et al. [28] showed that thermal neutrons induce transmutation of Al in Si which results in the formation of pure Si particles together with the dissolution of β'' due to fast neutrons. However, in the present study, the new particles form without transmutation, which rules out possible effects of Si enrichment.

5. Conclusions

In this work it has been demonstrated that β'' precipitates display a centered monoclinic structure and contain Mg, Si, Al and Cu with a Mg : Si ratio approaching 2, close to the ratio of the alloy. After 95 dpa ion irradiation, a decrease of size and a slight lattice distortion of β'' has been observed although the orientation with the matrix is unchanged. These modified β'' coexist with a new population of particles observed by dark field imaging along the [112] matrix direction. Irradiation up to 165 dpa induces the full dissolution of β'' whereas the new particles grow. TEM and APT observations have shown that these particles induced by ion irradiation do not belong to the β precipitation sequence and that they contain Mg, Si, Cu, Al and Cr. Their

formation is likely driven by solute release from the β'' precipitates and from the Cr-containing dispersoids, followed by a strong precipitation driving force of Mg and Si and their growth by solute drag by vacancies or interstitials process.

Acknowledgements:

This study was made in the frame of the MTRJH project. The CEA Saclay and CSNSM Orsay JANNuS facilities part of the EMIR network, the IM2NP part of the French CNRS (FR3507) and CEA METSA network are gratefully acknowledged. The authors thank F. De Geuser from SIMAP Grenoble for fruitful discussions.

References

[1] D. Iracane, P. Chaix, and A. Alamo, Jules Horowitz Reactor: a high performance material testing reactor, Mater. Subj. Fast Neutron Irradiat., 9 (2008) 445–456.

[2] S. J. Andersen, H. W. Zandbergen, J. Jansen, C. TrÆholt, U. Tundal, and O. Reiso, The crystal structure of the β″ phase in Al–Mg–Si alloys, Acta Mater., 46 (1998) 3283–3298.

[3] R. Vissers, M. A. van Huis, J. Jansen, H. W. Zandbergen, C. D. Marioara, and S. J. Andersen, The crystal structure of the β′ phase in Al–Mg–Si alloys, Acta Mater., 55 (2007) 3815–3823.

[4] S. J. Andersen, C. D. Marioara, R. Vissers, A. Frøseth, and H. W. Zandbergen, The structural relation between precipitates in Al–Mg–Si alloys, the Al-matrix and diamond silicon, with emphasis on the trigonal phase U1-MgAl2Si2, Mater. Sci. Eng. A, 444 (2007) 157–169.

[5] S. J. Andersen, C. D. Marioara, A. Frøseth, R. Vissers, and H. W. Zandbergen, Crystal structure of the orthorhombic U2-Al4Mg4Si4 precipitate in the Al–Mg–Si alloy system and its relation to the β′ and β″ phases, Mater. Sci. Eng. A, 390 (2005) 127–138.

[6] C. S. T. Chang, F. De Geuser, and J. Banhart, In situ characterization of β″ precipitation in an Al–Mg–Si alloy by anisotropic small-angle neutron scattering on a single crystal, J. Appl. Crystallogr., 48 (2015) 455–463.

[7] H. W. Zandbergen, S. J. Andersen, and J. Jansen, Structure Determination of Mg5Si6 Particles in Al by Dynamic Electron Diffraction Studies, Science, 277 (1997) 1221–1225.

[8] G. A. Edwards, K. Stiller, G. L. Dunlop, and M. J. Couper, The precipitation sequence in Al–Mg–Si alloys, Acta Mater., 46 (1998) 3893–3904.

[9] K. Matsuda, T. Naoi, K. Fujii, Y. Uetani, T. Sato, A. Kamio, and S. Ikeno, Crystal structure of the β″ phase in an Al–l.0mass%Mg2Si–0.4mass%Si alloy, Mater. Sci. Eng. A, 262 (1999) 232–237.

[10] P. M. Derlet, S. J. Andersen, C. D. Marioara, and A. Frøseth, A first-principles study of the β''-phase in Al-Mg-Si alloys, J. Phys. Condens. Matter, 14 (2012) 4011–4024.

[11] M. Murayama and K. Hono, Pre-precipitate clusters and precipitation processes in Al–Mg–Si alloys, Acta Mater., 47 (1999) 1537–1548.

[12] N. Maruyama, R. Uemori, N. Hashimoto, M. Saga, and M. Kikuchi, Effect of silicon addition on the composition and structure of fine-scale precipitates in Al-Mg-Si alloys, Scr. Mater., 36 (1997) 89–93.

[13] H. K. Hasting, W. Lefebvre, C. Marioara, J. C. Walmsley, S. Andersen, R. Holmestad, and F. Danoix, Comparative study of the β″-phase in a 6xxx Al alloy by 3DAP and HRTEM, Surf. Interface Anal., 39 (2007) 189–194.

[14] H. S. Hasting, A. G. Frøseth, S. J. Andersen, R. Vissers, J. C. Walmsley, C. D. Marioara, F. Danoix, W. Lefebvre, and R. Holmestad, Composition of β″ precipitates in Al–Mg–Si alloys by atom probe tomography and first principles calculations, J. Appl. Phys., 106 (2009) 123527 1–9.

[15] P. H. Ninive, A. Strandlie, S. Gulbrandsen-Dahl, W. Lefebvre, C. D. Marioara, S. J. Andersen, J. Friis, R. Holmestad, and O. M. Løvvik, Detailed atomistic insight into the β″ phase in Al–Mg–Si alloys, Acta Mater., 69 (2014) 126–134.

[16] C. D. Marioara, S. J. Andersen, T. N. Stene, H. Hasting, J. Walmsley, A. T. J. Van Helvoort, and R. Holmestad, The effect of Cu on precipitation in Al–Mg–Si alloys, Philos. Mag., 87 (2007) 3385–3413.

[17] L. Ding, Z. Jia, Z. Zhang, R. E. Sanders, Q. Liu, and G. Yang, The natural aging and precipitation hardening behaviour of Al-Mg-Si-Cu alloys with different Mg/Si ratios and Cu additions, Mater. Sci. Eng. A, 627 (2015) 119–126.

[18] K. Li, A. Béché, M. Song, G. Sha, X. Lu, K. Zhang, Y. Du, S. P. Ringer, and D. Schryvers, Atomistic structure of Cu-containing β″ precipitates in an Al–Mg–Si–Cu alloy, Scr. Mater., 75 (2014) 86–89.

[19] K. Teichmann, C. D. Marioara, S. J. Andersen, K. O. Pedersen, S. Gulbrandsen-Dahl, M. Kolar, R. Holmestad, and K. Marthinsen, HRTEM study of the effect of deformation on the early precipitation behavior in an AA6060 Al-Mg-Si alloy, Philos. Mag., 91 (2011) 3744–3754.

[20] M. Torsæter, W. Lefebvre, C. D. Marioara, S. J. Andersen, J. C. Walmsley, and R. Holmestad, Study of intergrown L and Q' precipitates in Al-Mg-Si-Cu alloys, Scr. Mater., 64 (2011) 817–820.

[21] L. Sagalowicz, G. Hug, D. Bechet, P. Sainfort, and G. Lapasset, 4th Int Conf Al Alloys Their Phys. Mech. Prop. Trans Tech Publ. Suisse, (1994) 636–643.

[22] D. J. Chakrabarti and D. E. Laughlin, Phase relations and precipitation in Al–Mg–Si alloys with Cu additions, Prog. Mater. Sci., 49 (2004) 389–410.

[23] M. Torsæter, F. J. H. Ehlers, C. D. Marioara, S. J. Andersen, and R. Holmestad, Applying precipitate-host lattice coherency for compositional determination of precipitates in Al-Mg-Si-Cu alloys, Philos. Mag., 92 (2012) 3833–3856.

[24] C. Flament, Study of microstructural evolutions of the 6061-T6 aluminium alloy under irradiation, PhD thesis, 2015.

[25] C. D. Marioara, H. Nordmark, S. J. Andersen, and R. Holmestad, Post-β″ phases and their influence on microstructure and hardness in 6xxx Al-Mg-Si alloys, J. Mater. Sci., 41 (2006) 471–478.

[26] C.-S. Tsao, C.-Y. Chen, U.-S. Jeng, and T.-Y. Kuo, Precipitation kinetics and transformation of metastable phases in Al–Mg–Si alloys, Acta Mater., 54 (2006) 4621–4631.

[27] K. Farrell and R. T. King, Tensile properties of neutron-irradiated 6061 alumnium alloy in annealed and precipitation-hardened conditions, ASTM STP 683, (1978) 440–449.

[28] J. R. Weeks, C. J. Czajkowski, and K. Farrell, Effects of high thermal neutron fluences on type 6061 aluminum, 16th International Symposium on the Effects of Radiation on Materials, 1992.

[29] R. T. King, A. Jostsons, and K. Farrell, Neutron Irradiation Damage in a Precipitation-Hardened Aluminum Alloy, ASTM-STP35444S, 1973.

[30] N. Chauvin, S. Henry, H. Flocard, F. Fortuna, O. Kaitasov, P. Pariset, S. Pellegrino, M. O. Ruault, Y. Serruys, and P. Trocelier, Optics calculations and beam line design for the JANNuS facility in Orsay, Appl. Accel. Res. Ind. Ninet. Int. Conf., 261 (2007) 34–39.

[31] http://www.csnsm.in2p3.fr/Equipements.

[32] L. Beck, Y. Serruys, S. Miro, P. Trocellier, É. Bordas, F. Leprêtre, D. Brimbal, T. Loussouarn, H. Martin, S. Vaubaillon, S. Pellegrino, and D. Bachiller-Perea, Ion

irradiation and radiation effect characterization at the JANNUS-Saclay triple beam facility, J. Mater. Res., 30 (2015) 1183–1194.

[33] J. F. Ziegler, J. Biersack, and U. Littmark, The stopping and range of ions in solid, Pergamon Press. New York, 1985.

[34] R. E. Stoller, M. B. Toloczko, G. S. Was, A. G. Certain, S. Dwaraknath, and F. A. Garner, On the use of SRIM for computing radiation damage exposure, Nucl. Instrum. Methods Phys. Res. Sect. B Beam Interact. Mater. At., 310 (2013) 75–80.

[35] H. H. Neely and W. Bauer, Electron-Irradiation Damage-Rate Measurements in Aluminum, Phys. Rev., 149 (1966) 535–539.

[36] P. Jung, Average atomic-displacement energies of cubic metals, Phys Rev B, 23 (1981) 664–670.

[37] D. J. Larson, T. J. Prosa, R. M. Ulfig, B. P. Geiser, and T. F. Kelly, Selected Analysis Topics, Local Electrode Atome Probe Tomography - a user's guide, Springer-Verlag New York, 2013.

[38] T. Mitsuda, I. Kobayashi, S. Kosugi, N. Fujita, Y. Saitoh, F. Hori, S. Semboshi, Y. Kaneno, K. Nishida, N. Soneda, and A. Iwase, Hardening of Al–Cu–Mg alloy by energetic ion irradiation, J. Nucl. Mater., 408 (2011) 201–204.

[39] J. Douin, P. Donnadieu, T. Epicier, G. Dirras, A. Proult, and J. Silvain, Stress field around precipitates: direct measurement and relation with the behavior of dislocations, Mater. Sci. Eng. A, 319–321 (2001) 270–273.

[40] W. Yang, M. Wang, R. Zhang, Q. Zhang, and X. Sheng, The diffraction patterns from β″ precipitates in 12 orientations in Al–Mg–Si alloy, Scr. Mater., 62 (2010) 705–708.

[41] F. De Geuser, Interpretation and processing of tomographic atom probe data: application to precipitation in Al-Mg-Si, PhD thesis, 2005.

[42] M. K. Miller and R. G. Forbes, Chapter 7: Data analysis, Atom-Probe Tomography : The Local Electrode Atom Probe, Springer-Verlag New York Inc, (2014) 303–345.

[43] T. Saito, C. D. Marioara, S. J. Andersen, W. Lefebvre, and R. Holmestad, Aberration-corrected HAADF-STEM investigations of precipitate structures in Al-Mg-Si alloys with low Cu additions, Philos. Mag., 94 (2014) 520–531.

[44] T. Saito, F. J. H. Ehlers, W. Lefebvre, D. Hernandez-Maldonado, R. Bjørge, C. D. Marioara, S. J. Andersen, E. A. Mørtsell, and R. Holmestad, Cu atoms suppress misfit dislocations at the β″/Al interface in Al–Mg–Si alloys, Scr. Mater., 110 (2016) 6–9.

[45] P. Bellon, Materials Science with ion beams, Springer-Verlag. Berlin: Bernas H., 2010.

[46] G. Martin, Phase stability under irradiation : ballistic effects, Phys. Rev. B, 30 (1984) 1424.

[47] K. H. Heinig, T. Müller, B. Schmidt, M. Strobel, and W. Möller, Interfaces under ion irradiation : growth and taming of nanostructures, Appl. Phys. A, 77 (2003) 17–25.

[48] G. Was, Fundamentals of Radiation Materials Science -Metals and alloys, Springer-Verlag. 2007.

[49] W. Gorecki and T. Gorecki, Vacancy migration energy in aluminium as determined from exoelectron emission measurements, Cryst. Res. Technol., 20 (1985) 111–114.

[50] A. D. Brailsford and L. K. Mansur, The effect of precipitate-matrix interface sinks on the growth of voids in the matrix, J. Nucl. Mater., 104 (1981) 1403–1408.

[51] S. M. Kim and W. J. L. Buyers, Temperature dependence of the vacancy formation energy in aluminum and positron annihilation, Phys. Lett. A, 49 (1974) 181–182.

[52] Y. Du, Y. Chang, B. Huang, W. Gong, Z. Jin, H. Xu, Z. Yuan, Y. Liu, Y. He, and F.-Y. Xie, Diffusion coefficients of some solutes in fcc and liquid Al: critical evaluation and correlation, Mater. Sci. Eng. A, 363 (2003) 140–151.

[53] C. Wolverton, Solute-vacancy binding in aluminium, Acta Mater., 55 (2007) 5867–5872.

[54] D. Simonovic and M. H. F. Sluiter, Impurity diffusion activation energies in Al from first principles, Phys. Rev. B, 79 (2009) 054304.

[55] M. Mantina, Y. Wang, L. Q. Chen, Z. K. Liu, and C. Wolverton, First principles impurity diffusion coefficients, Acta Mater., 57 (2009) 4102–4108.

[56] C. Flament, J. Ribis, J. Garnier, T. Vandenberghe, J. Henry, and A. Deschamps, Electron irradiation-enhanced core/shell organization of Al(Cr,Fe,Mn)Si dispersoids in Al-Mg-Si alloys, Philos. Mag., 95 (2015) 906–917.

[57] T. P. C. Klaver and J. H. Chen, Density functionnal theory study of alloy element interstitials in Al, J. Comput.-Aided Mater. Des., 10 (2003) 155–162.

[58] D. Ueyama, Y. Saitoh, F. Hori, Y. Kaneno, K. Nishida, K. Dohi, N. Soneda, S. Semboshi, and A. Iwase, Effects of energetic heavy ion irradiation on hardness of Al–Mg–Si alloys, Eighth Int. Symp. Swift Heavy Ions Matter SHIM 2012, 314 (2013) 107–111.

Figure captions:

Figure 1. Depth profile of displacement damage and ions concentration profile of 4MeV Au^{2+} and 2 MeV W^{3+} ions in Al calculated by SRIM.

Figure 2. Microstructure of the un-irradiated alloy. (a) Diffraction pattern of the 6061-T6 Al alloy oriented along the [100] zone axis, diffuse streaks (drawn in orange) correspond to β''-type precipitates. (b) Dark Field image produced by the selection of diffuse streaks by the contrast aperture.

Figure 3. Crystallographic structure of β'' nano-phases. (a) HRTEM micrograph of a nano-phase oriented parallel to the electron beam. (b) Filtered image of (a) with the Al atoms of the matrix lattice drawn in blue and Mg of the precipitate lattice in orange. (c) FFT associated to (b). (d) Simulated diffractogram of a centered monoclinic structure oriented along the [010] zone axis compared to (c) (with CaRIne 3.1).

Figure 4. Crystallographic structure of β'' nano-phases. (a) HRTEM micrograph of a nano-phase oriented perpendicularly to the electron beam. (b) FFT associated to (a). (d) Simulated diffractogram of a centered monoclinic structure oriented along the [001] zone axis compared to (c).

Figure 5. APT reconstruction from the un-irradiated Al 6061-T6 aluminum alloy (60x60x70 nm^3) (see Table 2 for clusters identification parameters).

Figure 6. *In situ* annealing of the 6061-T6 Al alloy along $[100]_{Al}$ zone axis. (a) BF image at room temperature. (b) at 200 °C. (c) at 240°C. (d) at 270°C.

Figure 7. Distribution of precipitate radiuses after thermal annealing of 6061-T6 to different temperatures.

Figure 8. Microstructure of the 6061-T6 Al alloy after 95 dpa irradiation at room temperature. (a) Diffraction pattern of the 6061-T6 alloy oriented along the [100] zone axis, diffuse streaks (drawn in orange) correspond to β''-type precipitates. (b) Dark field image produced by the selection of diffuse streaks by the contrast aperture.

Figure 9. Evolution of β'' nano-precipitates size under irradiation. (a) Equivalent radius of nano-precipitates before and after 95 dpa irradiation. (b) Length of nano-precipitates before and after 95 dpa irradiation.

Figure 10. Crystallographic structure of β'' nano-phases after 95 dpa irradiation. (a) HRTEM micrograph of a nano-phase oriented along the electron beam. (b) Filtered image of (a) with the Al atoms of the matrix lattice drawn in blue and Mg of the precipitate lattice in orange. (c) FFT associated to (b). (d) Simulated diffractogram of a centered monoclinic structure oriented along the [010] zone axis compared to (c) (with CaRIne 3.1).

Figure 11. Microstructure of the 6061-T6 Al alloy after 165 dpa at room temperature. (a) Diffraction pattern of the 6061-T6 alloy oriented along the [100] zone axis. (b) Dark field image produced by the selection of forbidden spots of Al by the contrast aperture (red circle on (a)).

Figure 12. Microstructure of the 6061-T6 alloy along the [112] zone axis. (a) DF image and diffraction pattern before irradiation. (b) DF image and diffraction pattern after 95 dpa irradiation. (c) DF image and diffraction pattern after 165 dpa irradiation.

Figure 13. APT reconstruction of the 6061-T6 Al alloy after 165 dpa irradiation (60x60x120 nm^3) (see table 2 for reconstruction parameters).

Figure 14. Crystallographic structure of the new precipitates formed under 165 dpa irradiation in the material. (a) High Resolution image. (b) Indexed FFT of (a).

Figure 15. Fit of λ to TRIM calculations of ion beam mixing of Si and Mg atoms from a 5 nm thick (Mg_2Si) precipitate surrounded by Al matrix under W^{3+} (2MeV) irradiation.

Figure 16. TEM-EDX maps of Mg, Si, Cu, Al and Cu atoms after 165 dpa irradiation, showing Mg and Si segregation at a grain boundary.

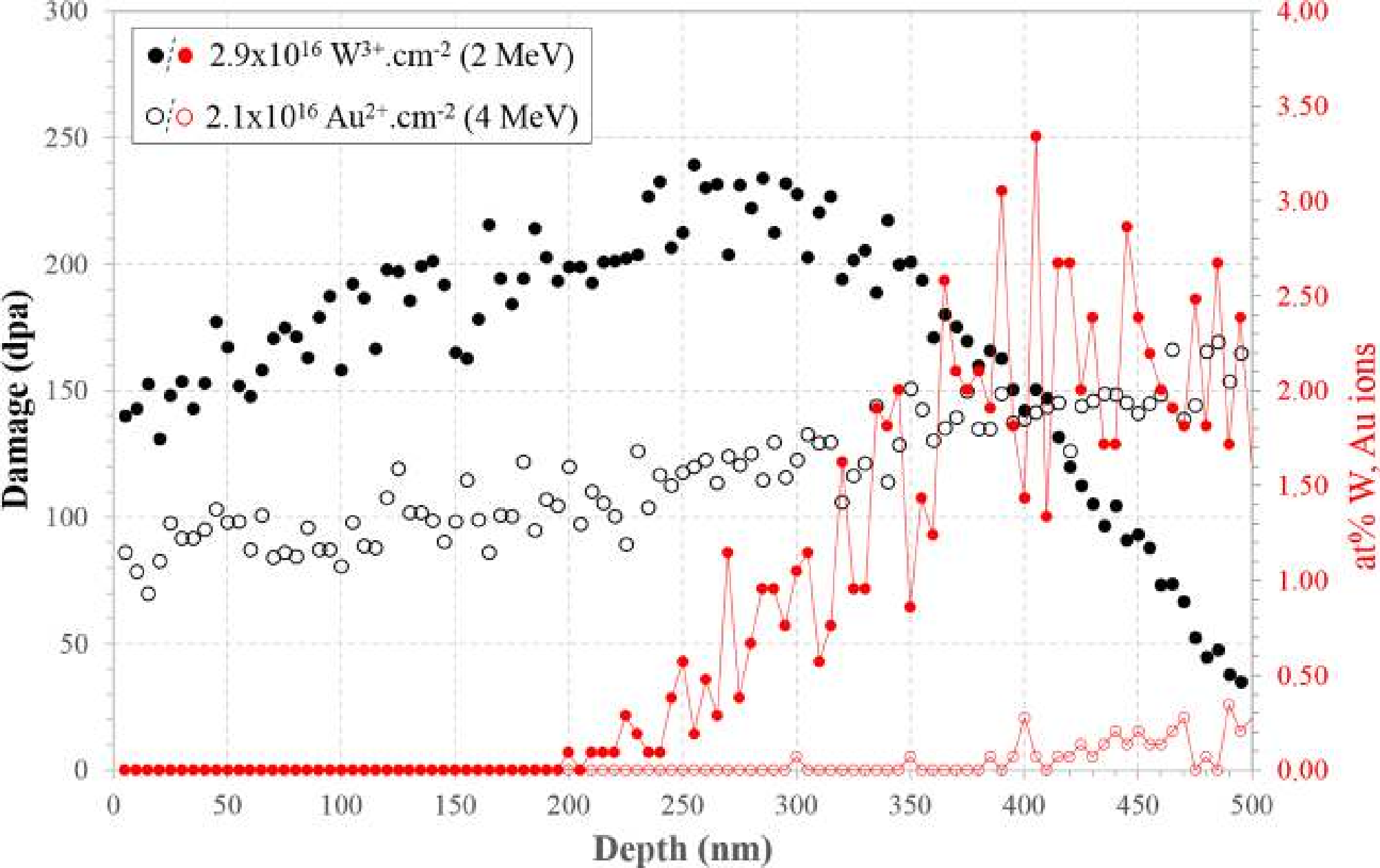
2.9x10^16 W^3+.cm^-2 (2 MeV)
2.1x10^16 Au^2+.cm^-2 (4 MeV)
Damage (dpa)
at% W, Au ions
Depth (nm)
0
50
100
150
200
250
300
350
400
450
500
0.00
0.50
1.00
1.50
2.00
2.50
3.00
3.50
4.00

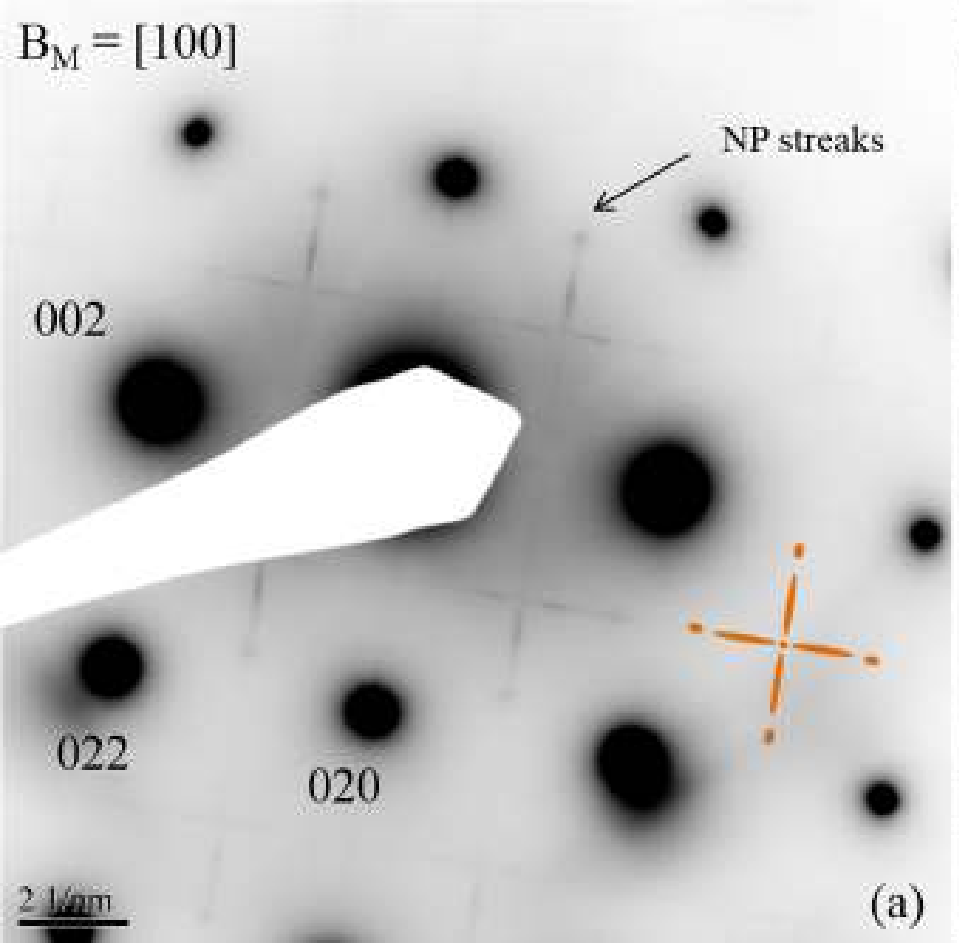
B_M = [100]
NP streaks
002
022
020
2 1/nm
(a)

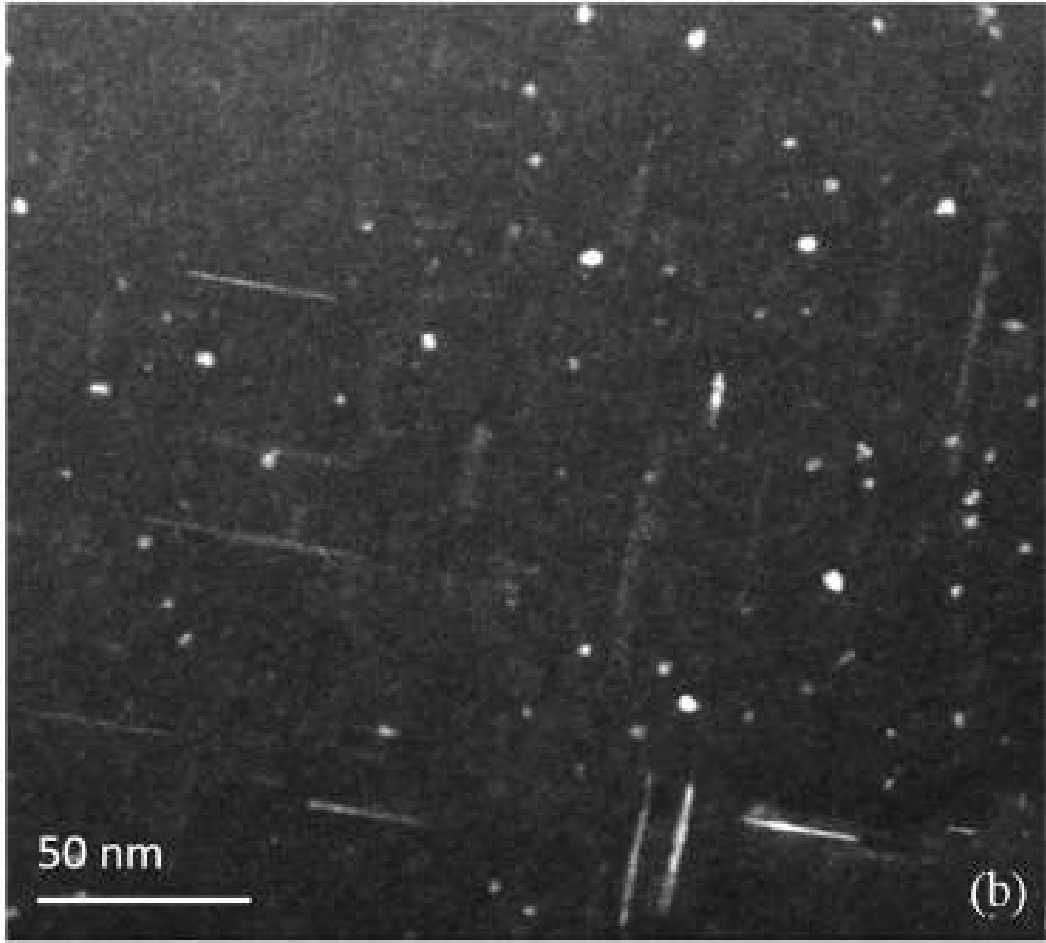
50 nm
(b)

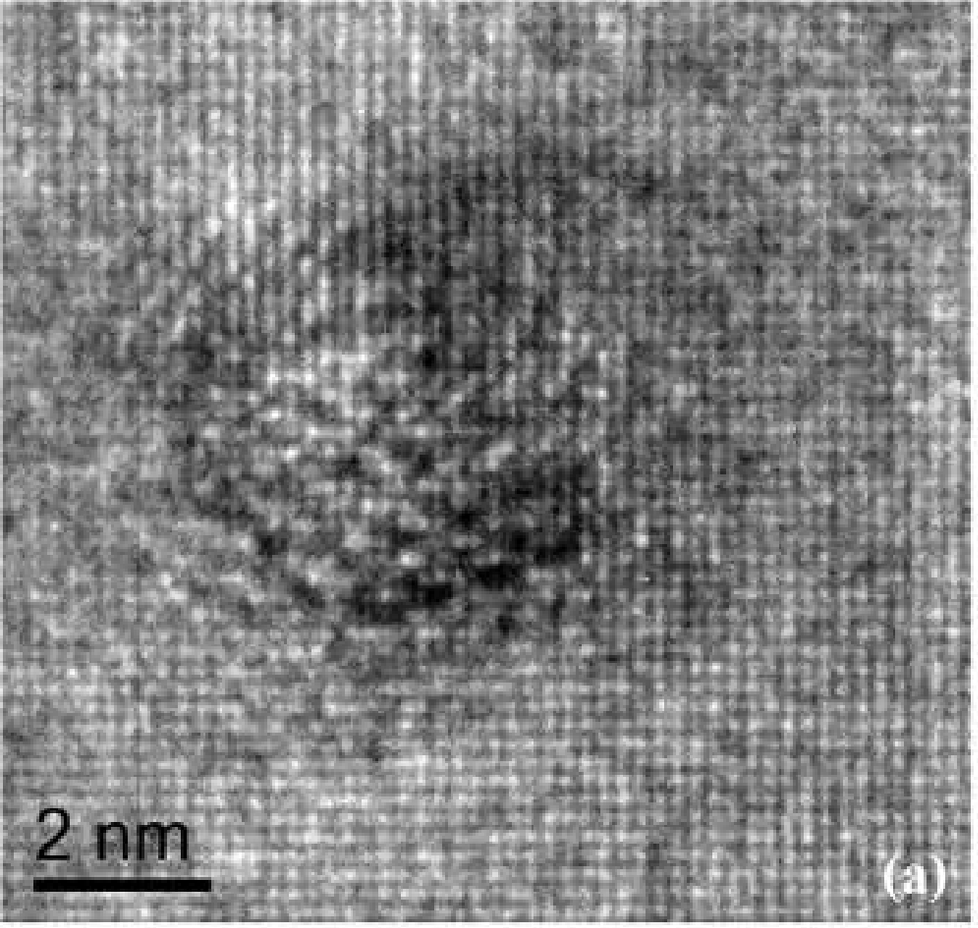
2 nm
(a)

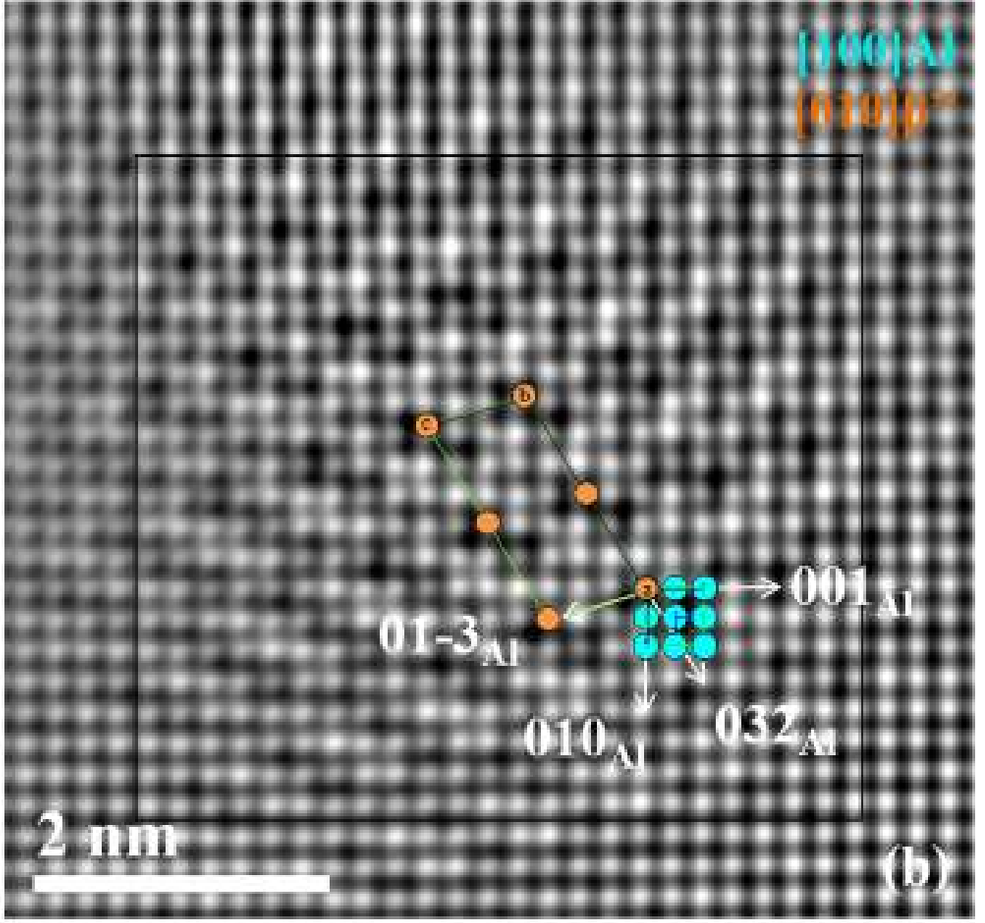
[100]Al
001Al
01-3Al
010Al
032Al
2 nm
(b)

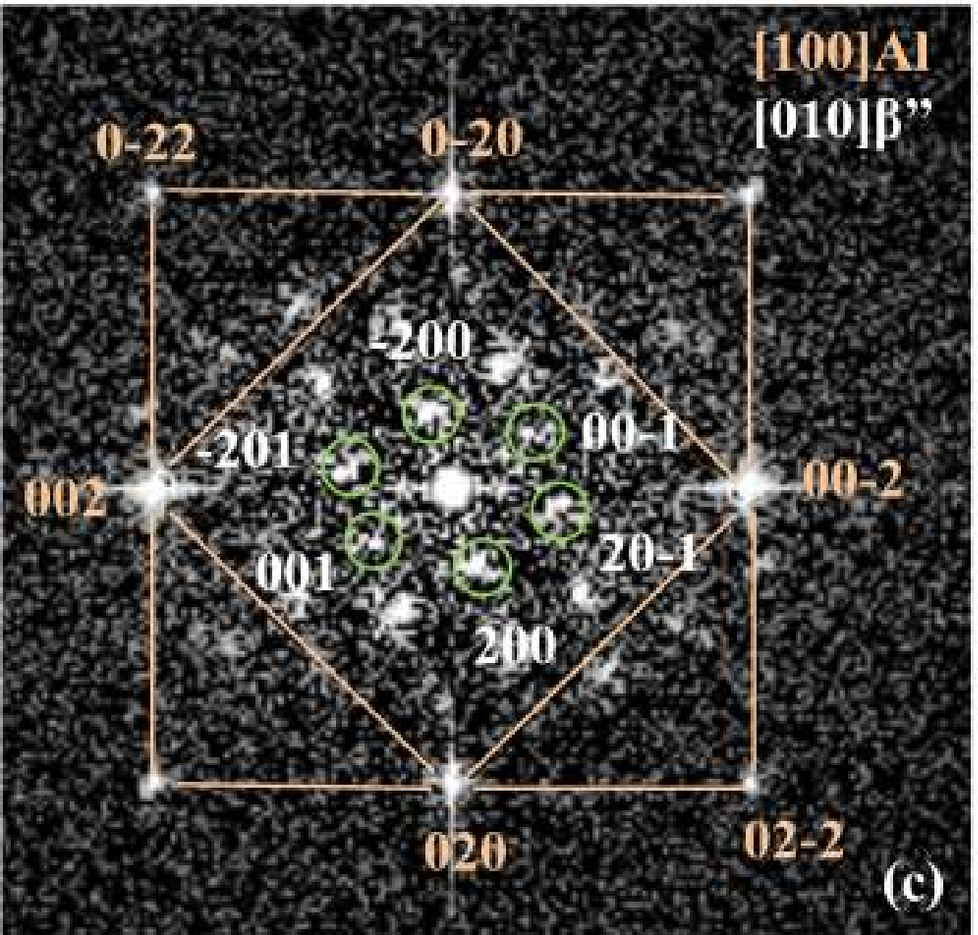
[100]Al
[010]β”
0-22
0-20
-200
-201
00-1
002
00-2
001
20-1
200
020
02-2
(c)

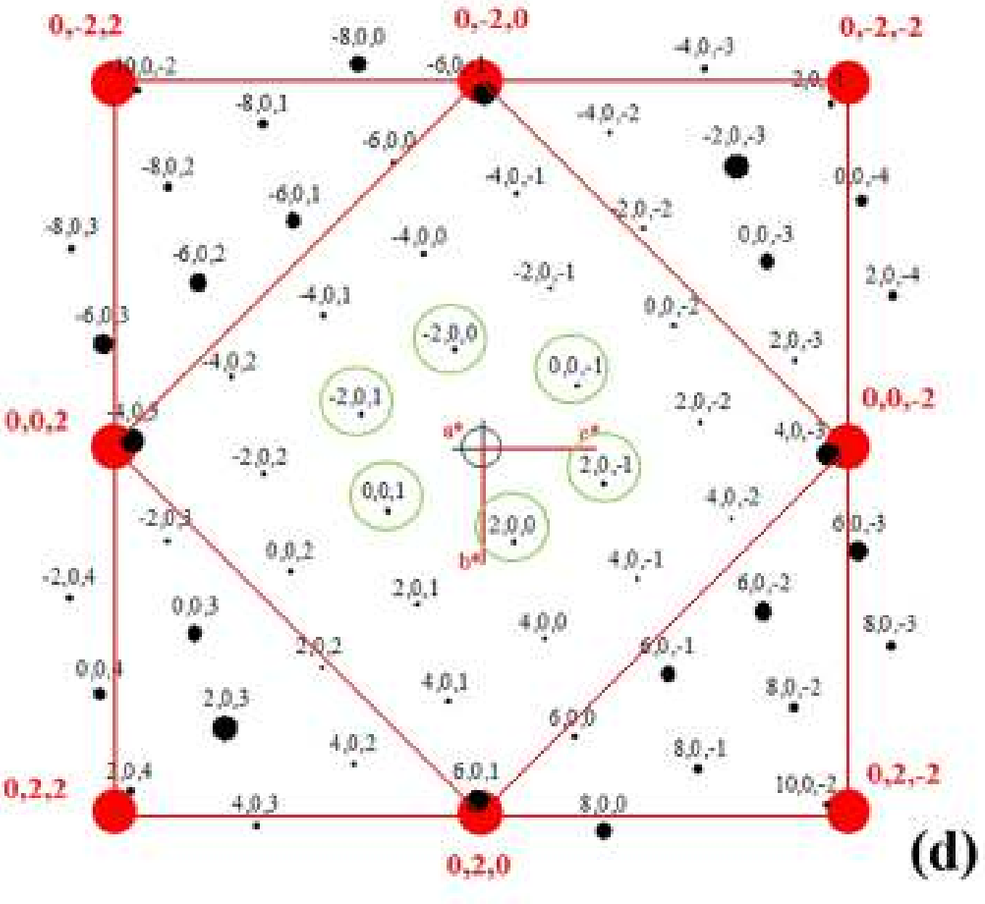
0,-2,2
0,-2,0
0,-2,-2
0,0,2
0,0,-2
0,2,2
0,2,0
0,2,-2
(d)

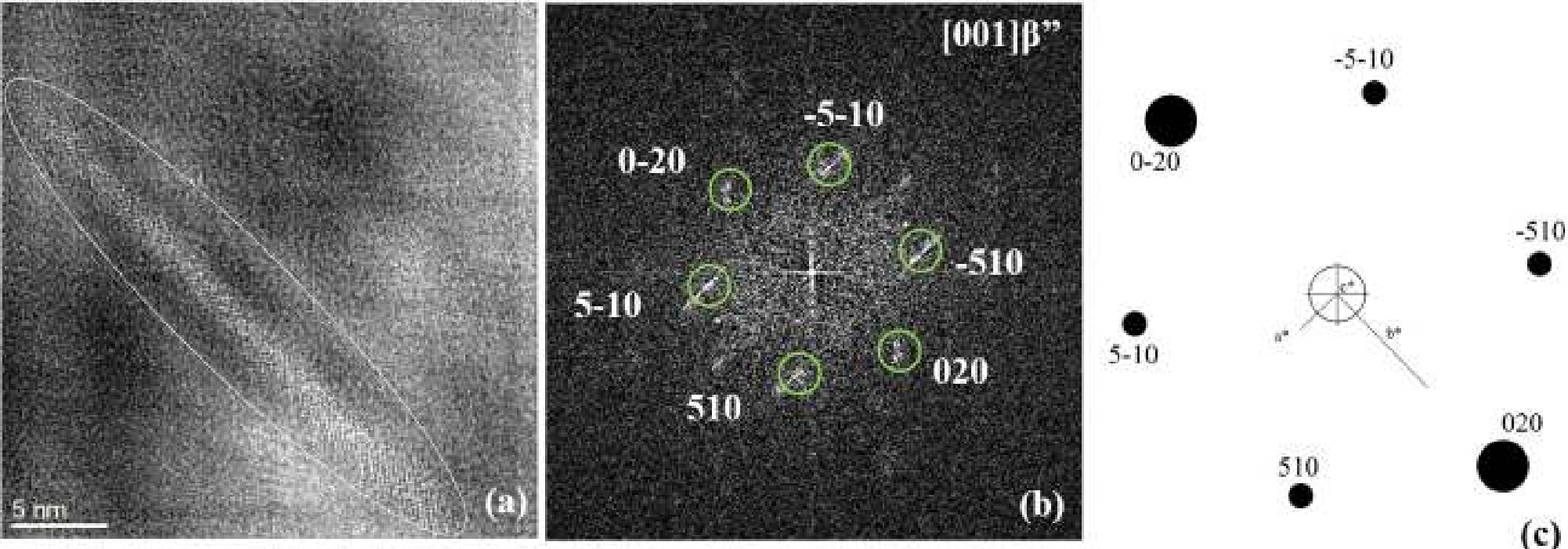
5 nm
(a)
[001]β"
-5-10
0-20
-510
5-10
020
510
(b)
-5-10
0-20
-510
5-10
020
510
(c)

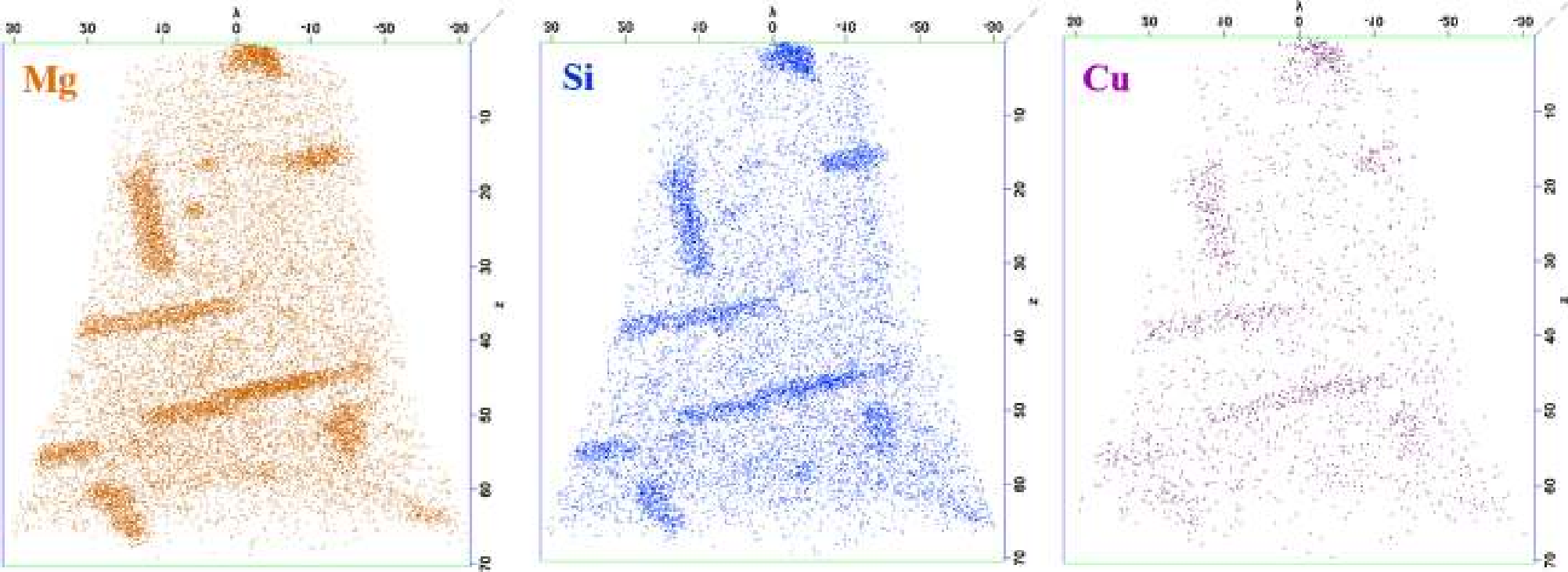
Mg
Si
Cu

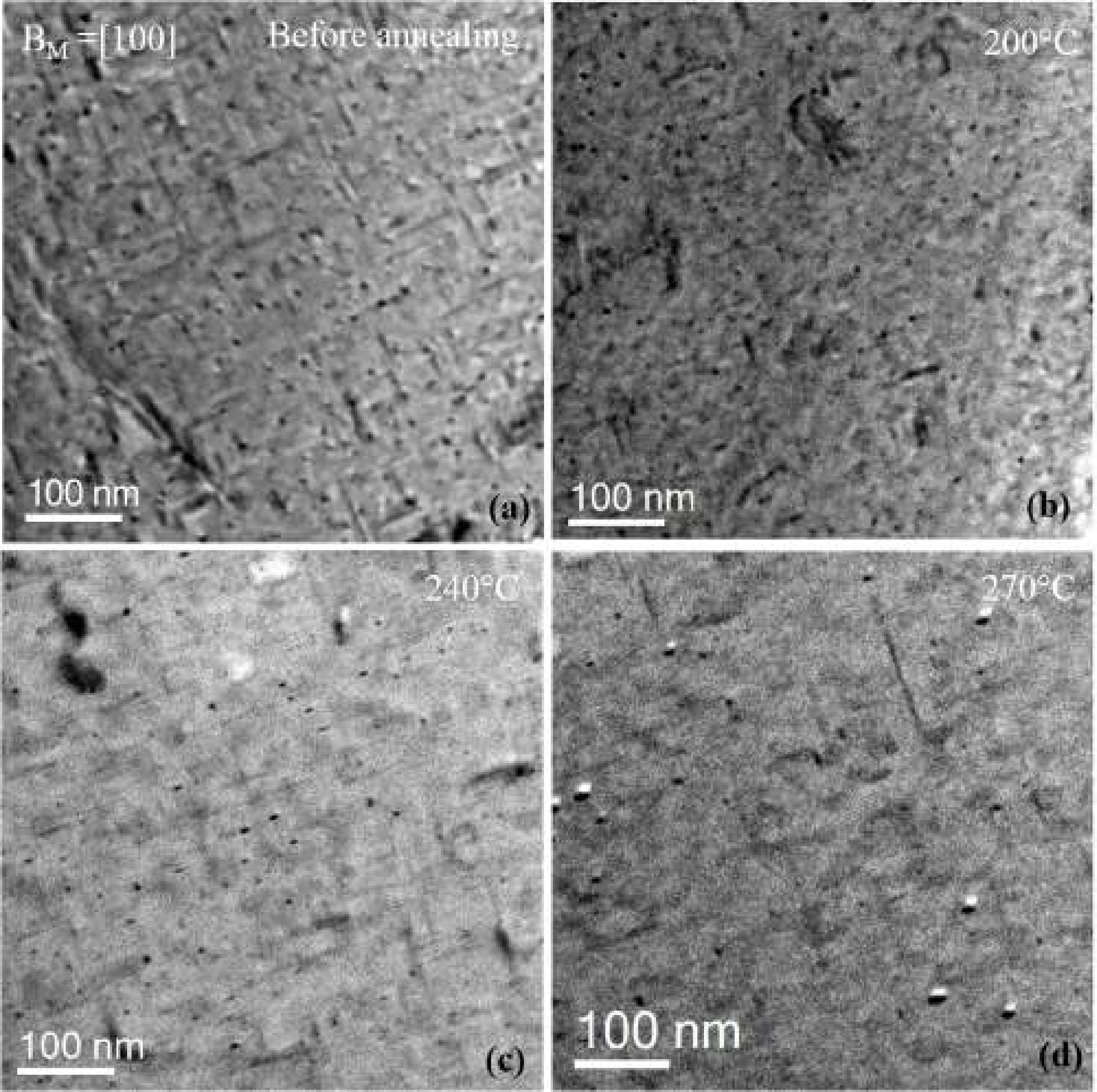
B_M =[100]
Before annealing
100 nm
(a)
200°C
100 nm
(b)
240°C
100 nm
(c)
270°C
100 nm
(d)

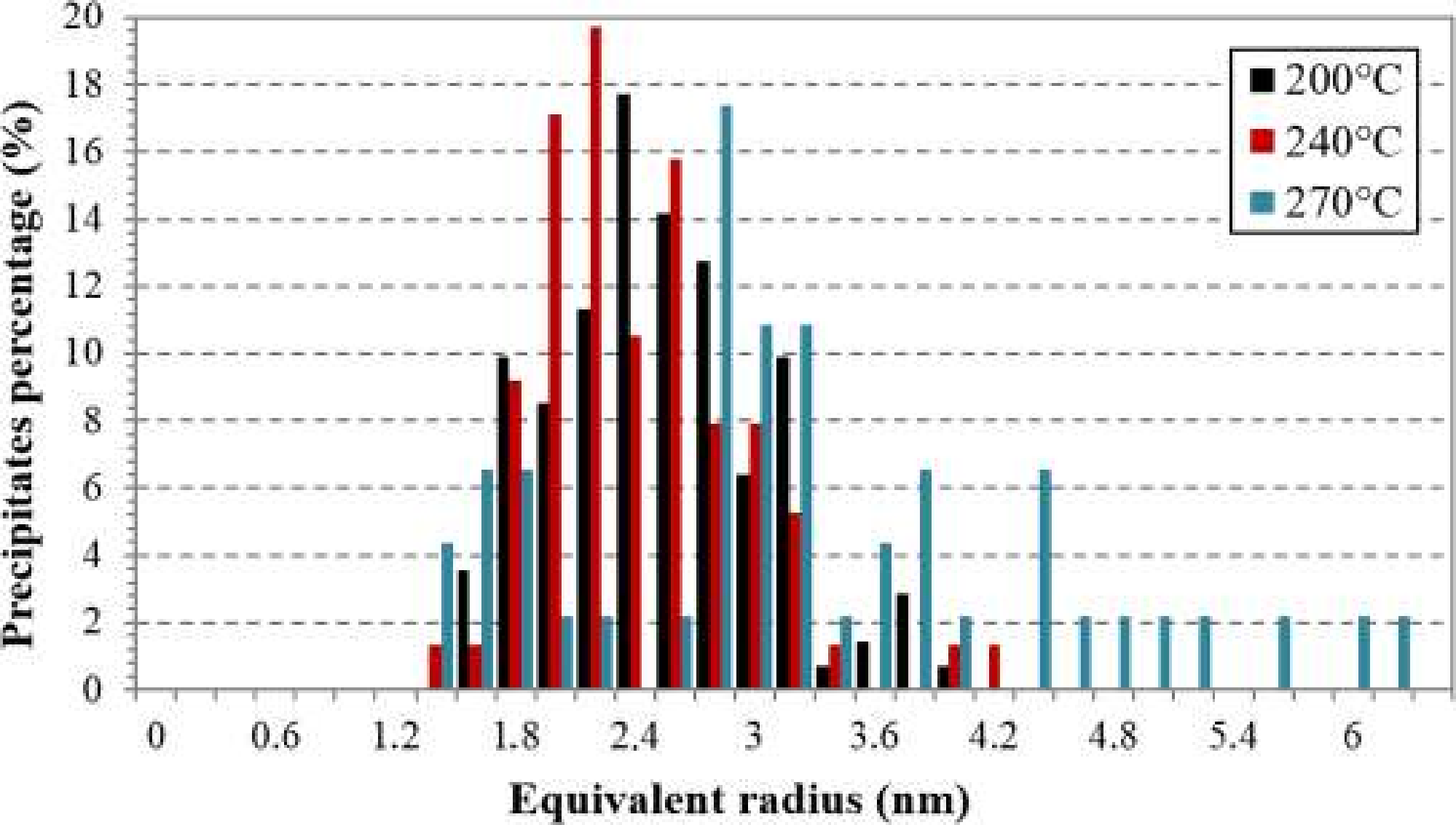
Precipitates percentage (%)
20
18
16
14
12
10
8
6
4
2
0
0
0.6
1.2
1.8
2.4
3
3.6
4.2
4.8
5.4
6
Equivalent radius (nm)
200°C
240°C
270°C

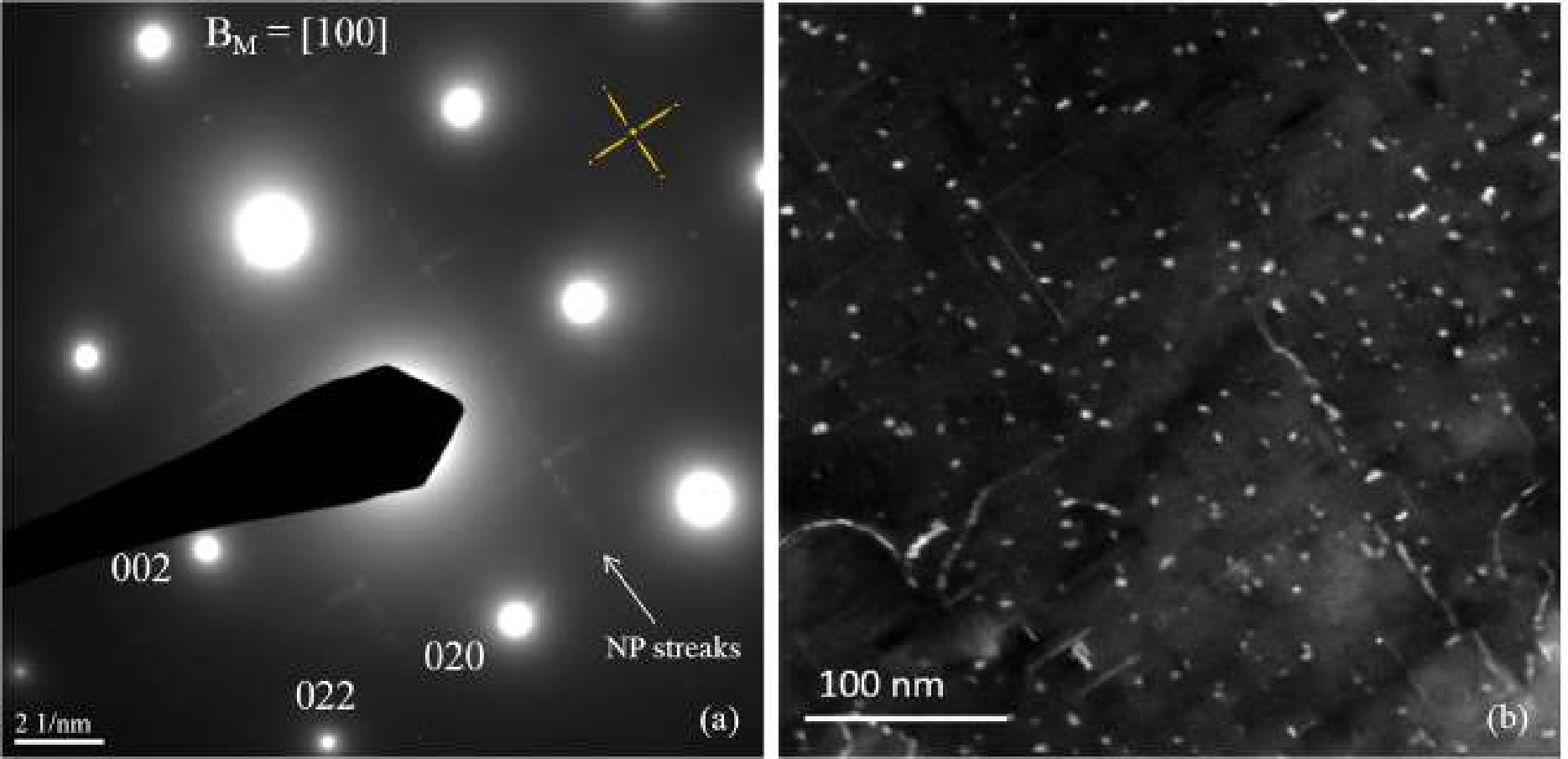
B_M = [100]
002
020
022
NP streaks
2 1/nm
(a)
100 nm
(b)

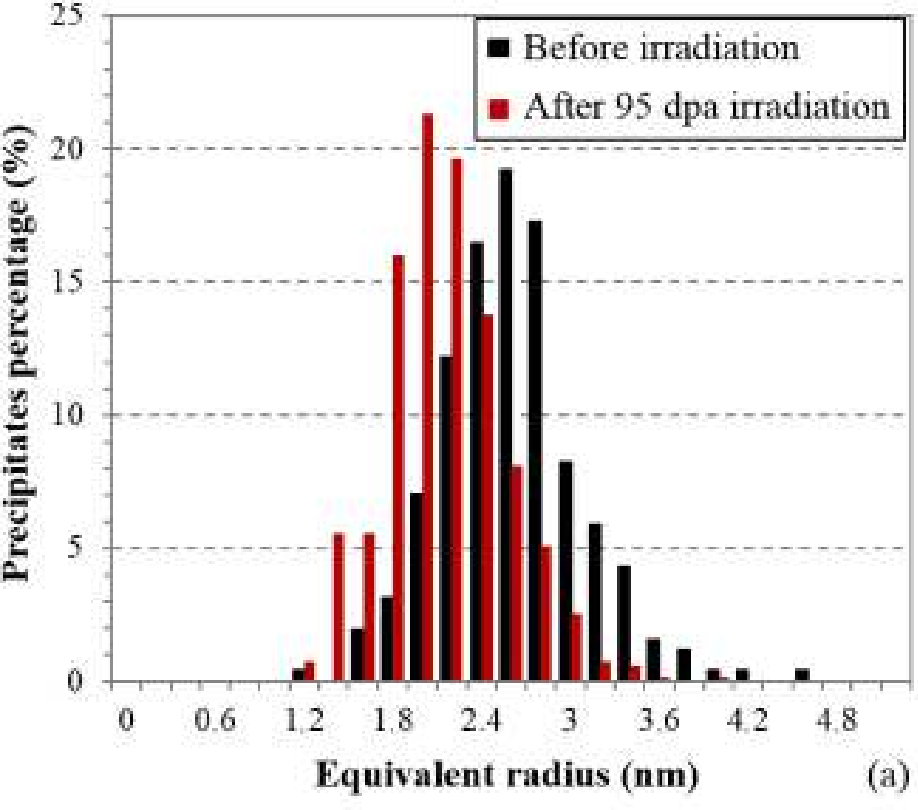
Before irradiation
After 95 dpa irradiation
Precipitates percentage (%)
0
5
10
15
20
25
0
0.6
1.2
1.8
2.4
3
3.6
4.2
4.8
Equivalent radius (nm)
(a)

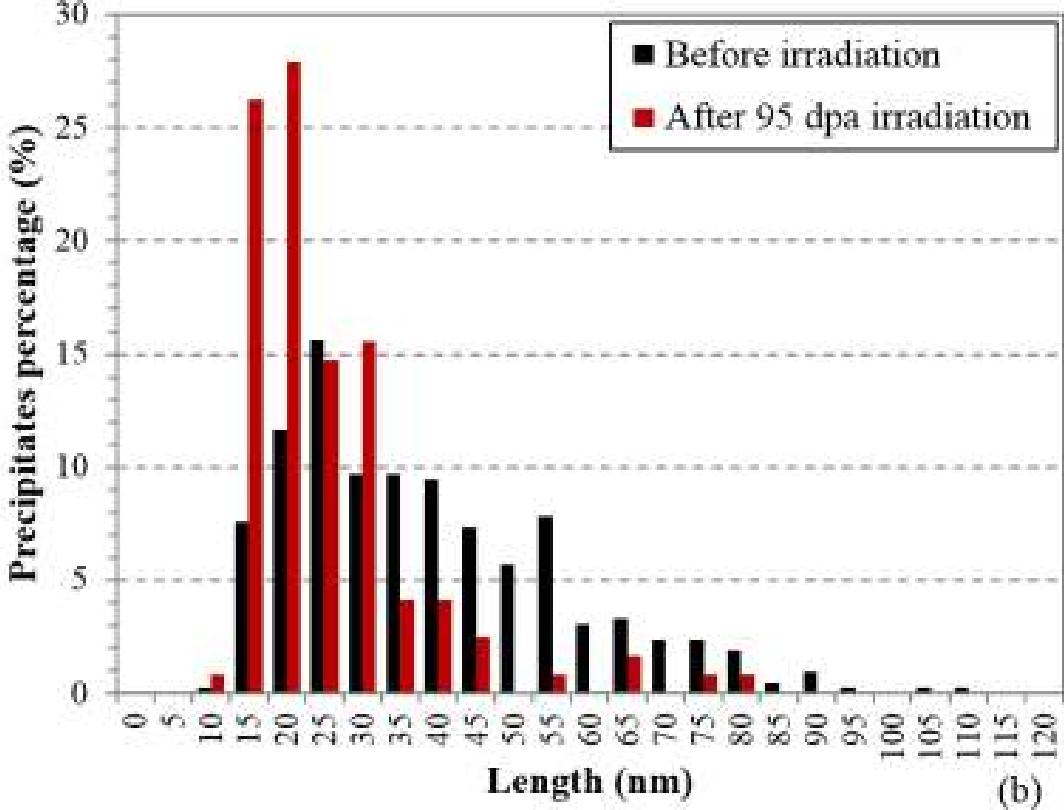
Before irradiation
After 95 dpa irradiation
Precipitates percentage (%)
0
5
10
15
20
25
30
0
5
10
15
20
25
30
35
40
45
50
55
60
65
70
75
80
85
90
95
100
105
110
115
120
Length (nm)
(b)

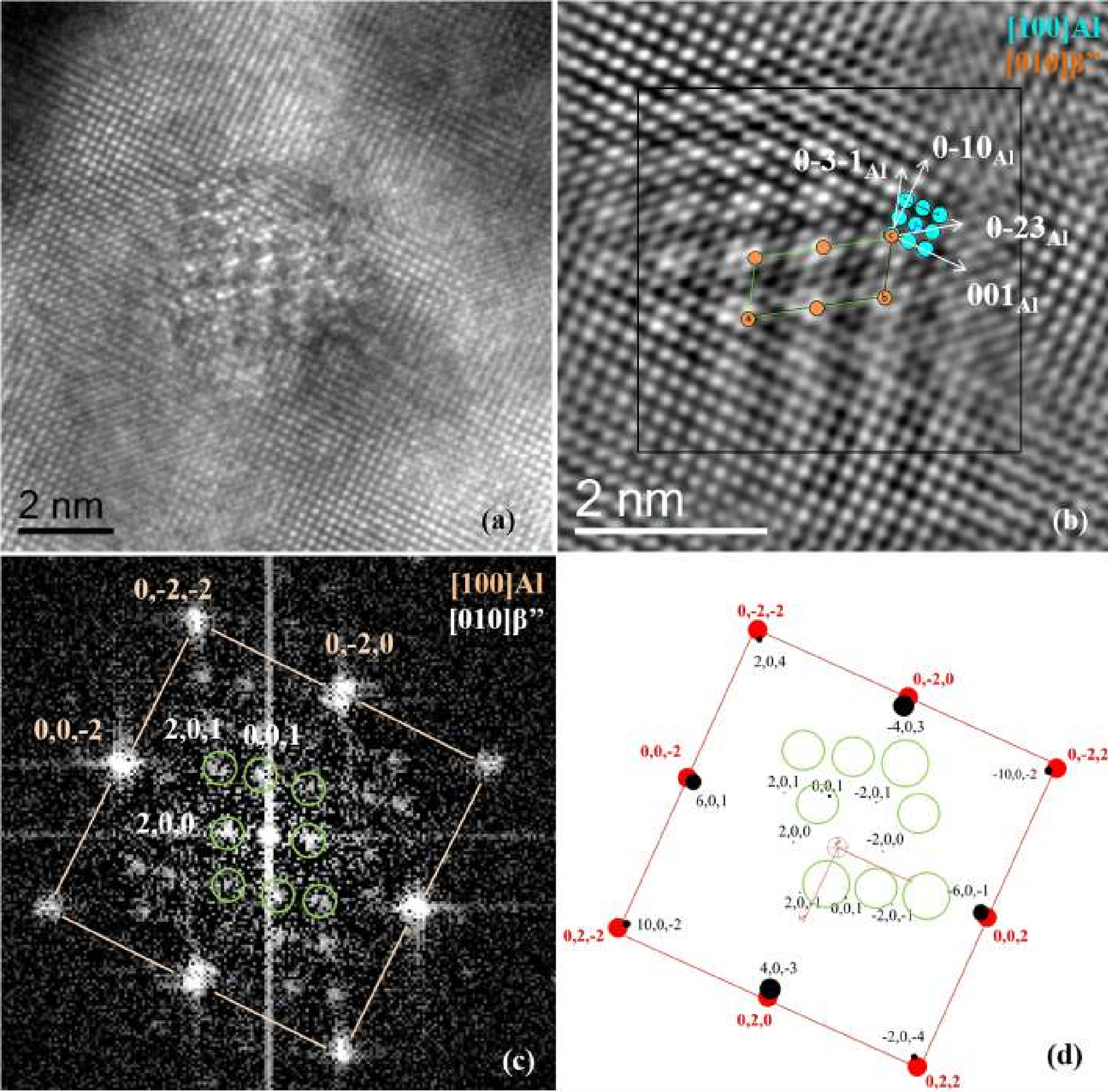
2 nm
(a)
[100]Al
[010]β"
0-3-1Al
0-10Al
0-23Al
001Al
2 nm
(b)
0,-2,-2
0,-2,0
0,0,-2
2,0,1
0,0,1
2,0,0
[100]Al
[010]β"
(c)
0,-2,-2
2,0,4
0,-2,0
-4,0,3
0,0,-2
6,0,1
0,-2,2
-10,0,-2
2,0,1
0,0,1
-2,0,1
2,0,0
-2,0,0
6,0,-1
2,0,-1
0,0,1
-2,0,-1
0,2,-2
10,0,-2
0,0,2
4,0,-3
0,2,0
-2,0,-4
0,2,2
(d)

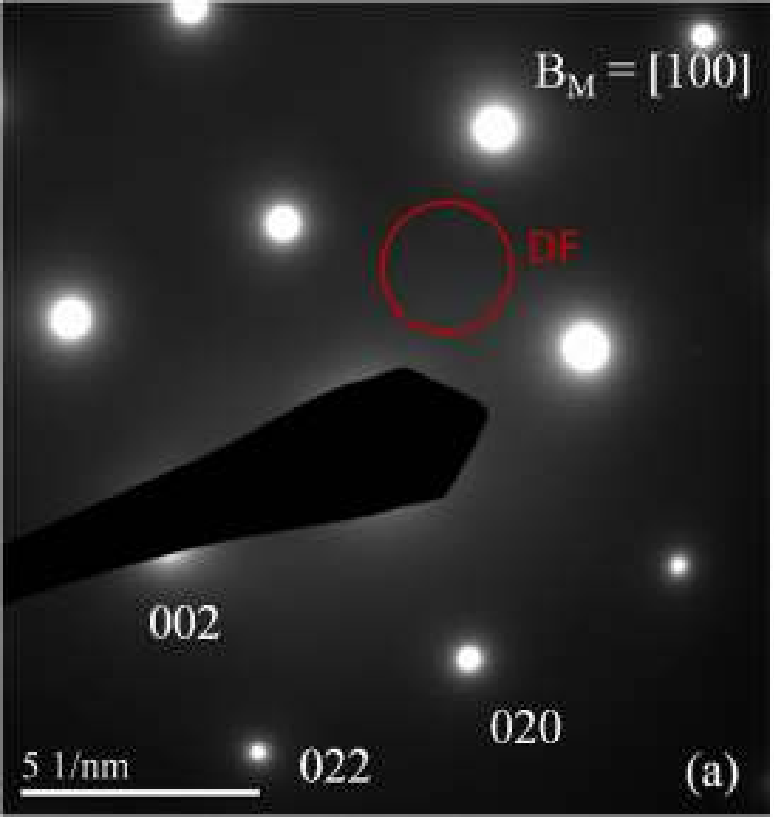
$B_M = [\bar{1}00]$
DF
002
020
022
5 1/nm
(a)

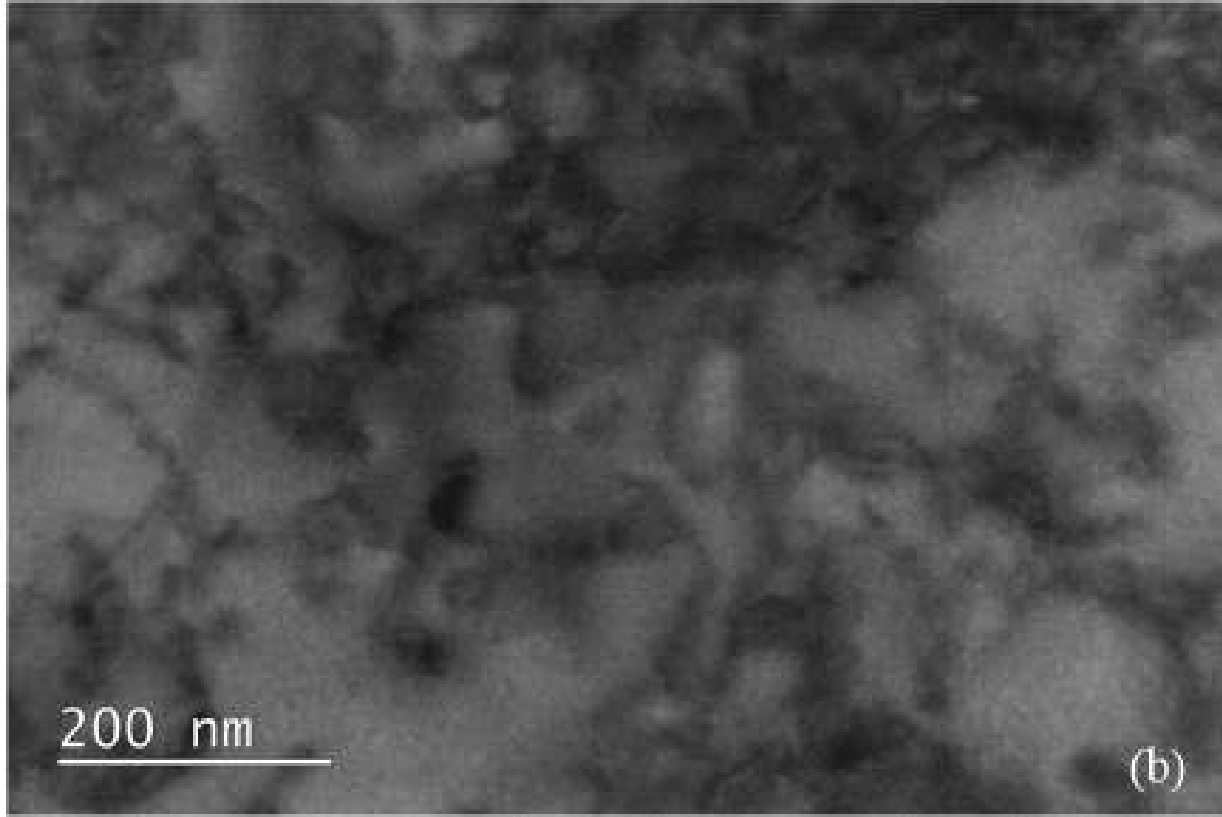
200 nm
(b)

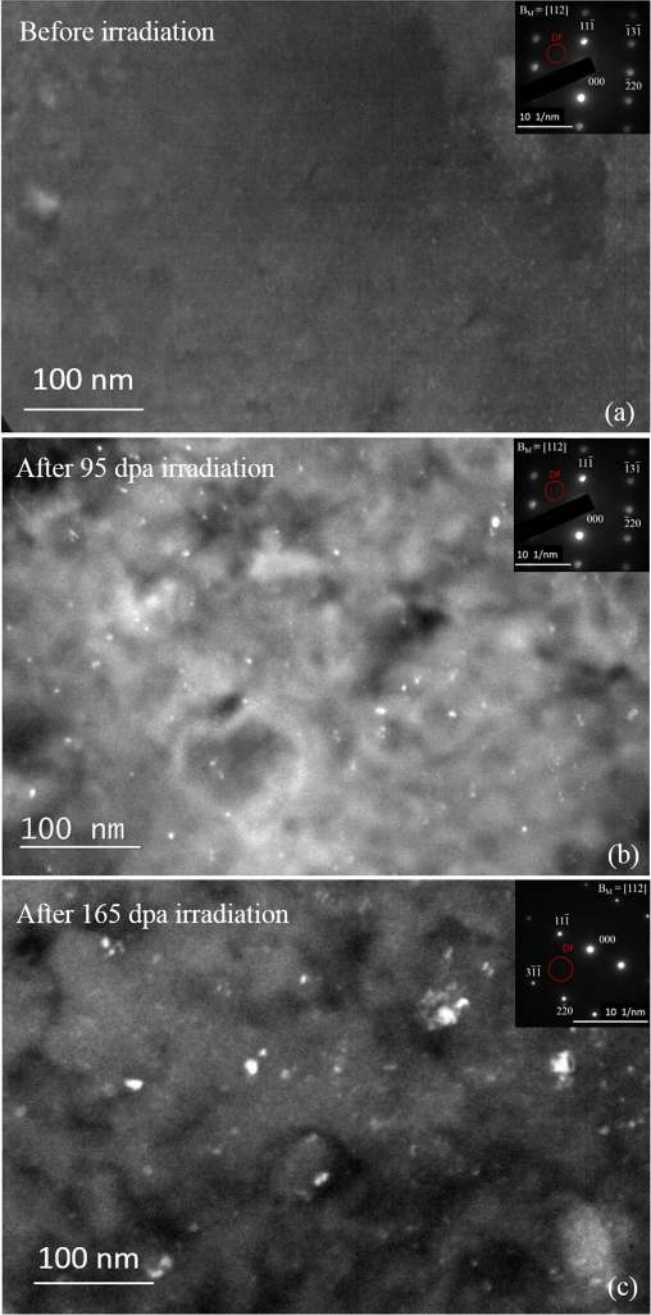
Before irradiation
100 nm
(a)
After 95 dpa irradiation
100 nm
(b)
After 165 dpa irradiation
100 nm
(c)

Al
Mg
Si
Cu
Cr
y
z
30
20
10
0
-10
-20
-30
100
80
60
40
20

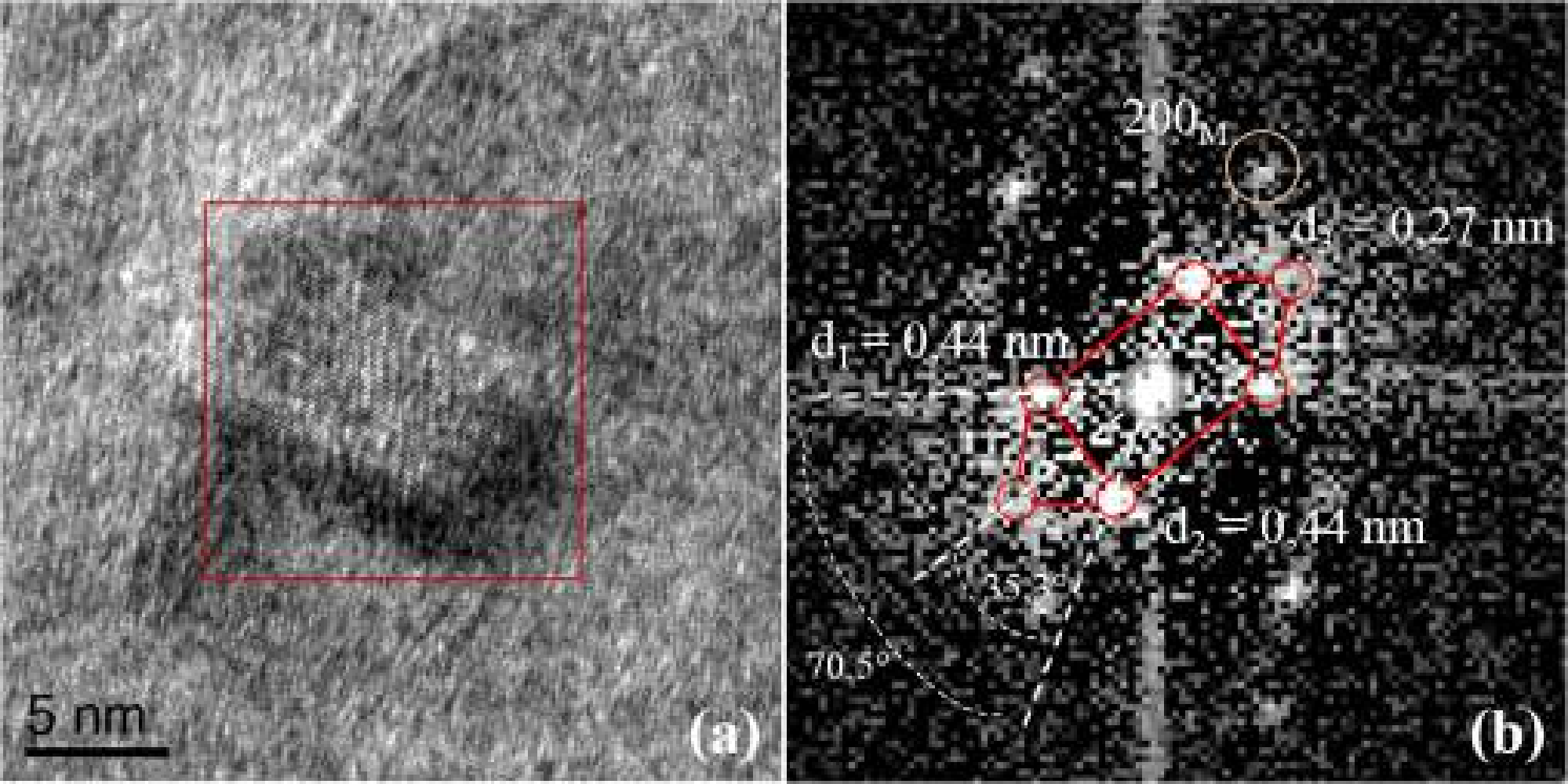
5 nm
(a)
200M
d3 = 0,27 nm
d1 = 0,44 nm
d2 = 0,44 nm
35,3°
70,5°
(b)

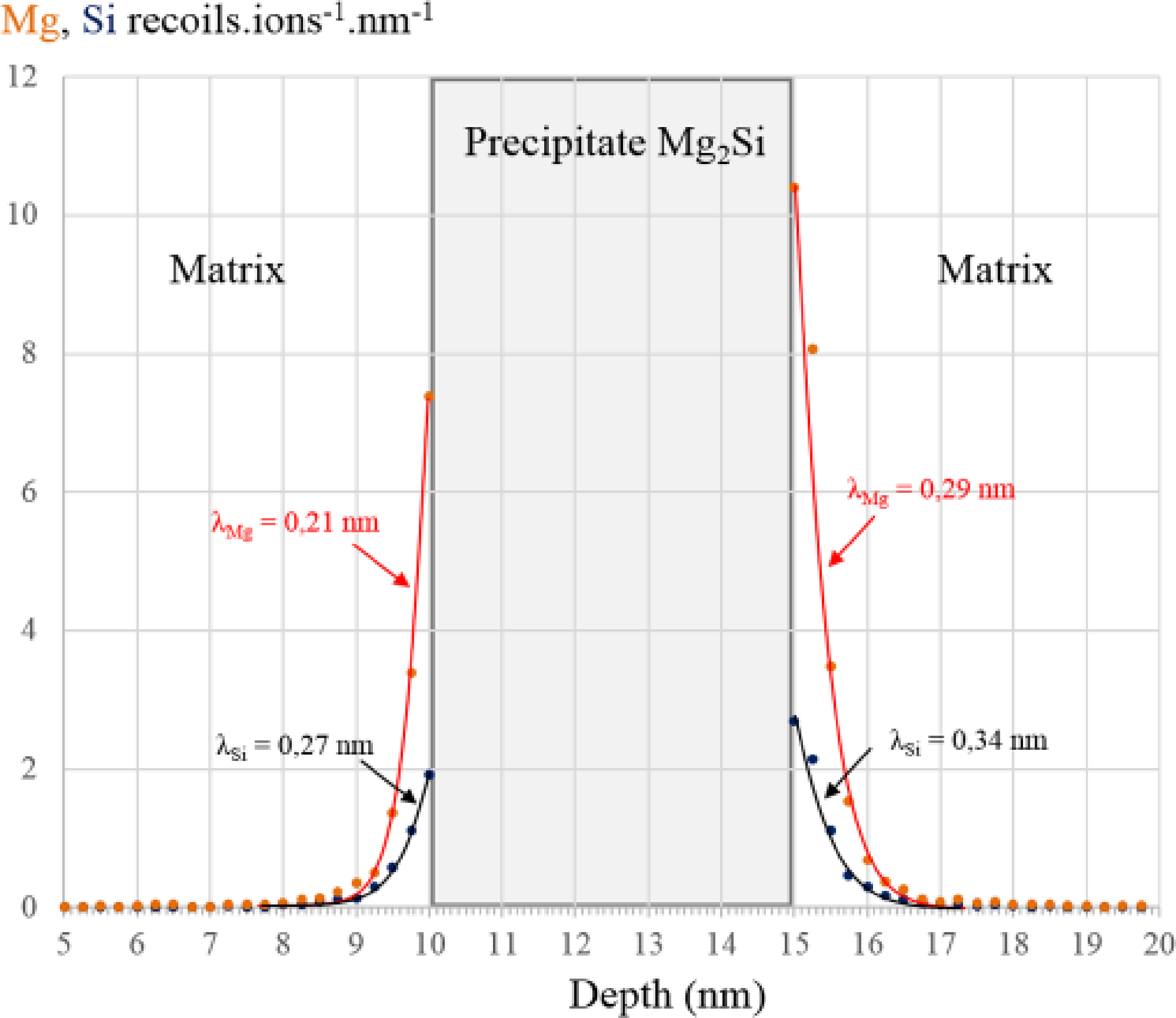
Mg, Si recoils.ions-1.nm-1
Precipitate Mg2Si
Matrix
Matrix
λMg = 0,21 nm
λMg = 0,29 nm
λSi = 0,27 nm
λSi = 0,34 nm
Depth (nm)

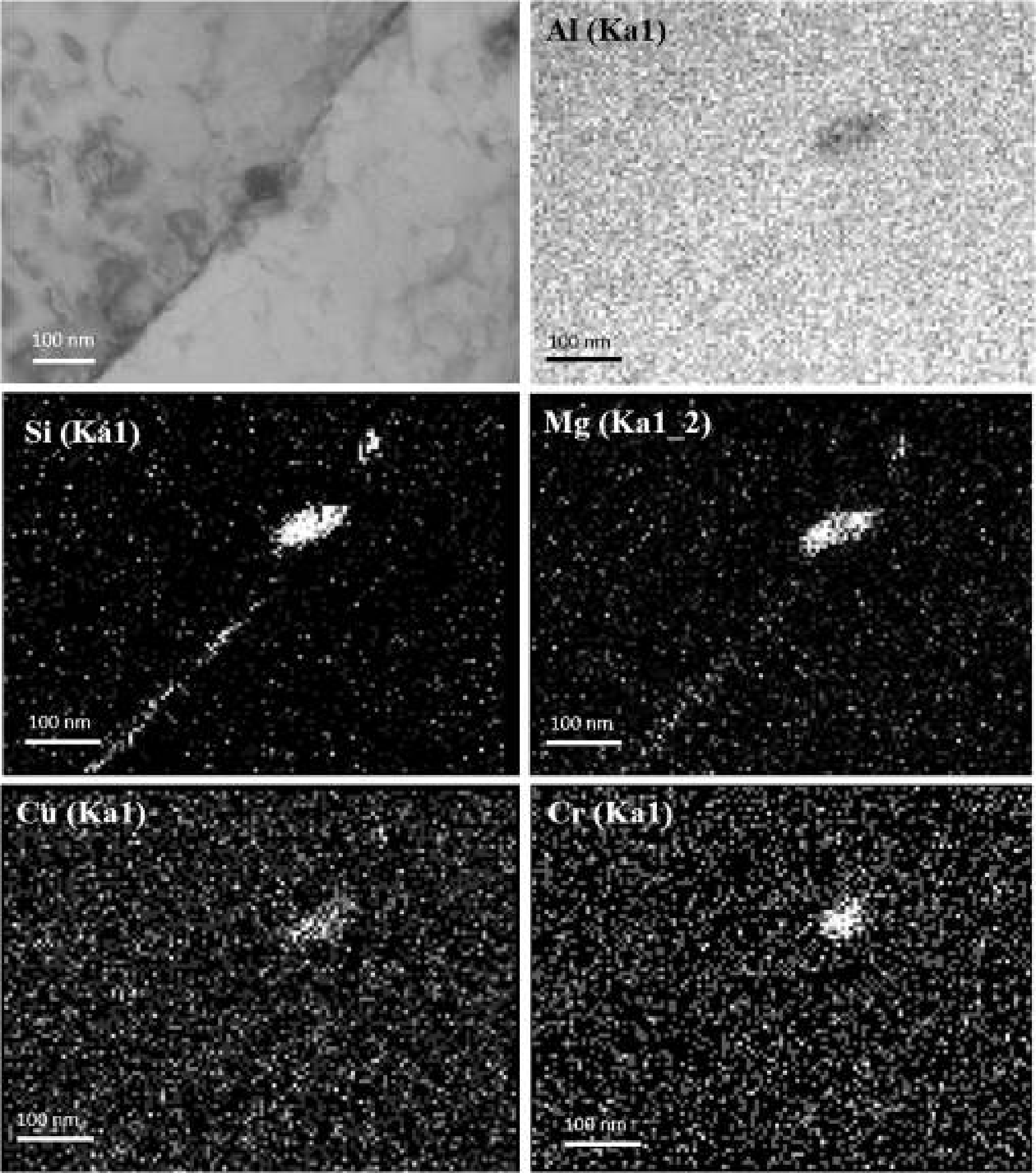
100 nm
Al (Ka1)
100 nm
Si (Ká1)
100 nm
Mg (Ka1_2)
100 nm
Cu (Ka1)
100 nm
Cr (Ka1)
100 nm

β'' nano-phases

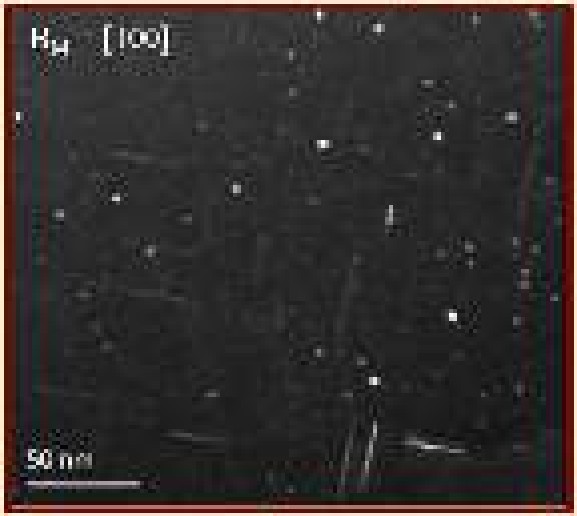

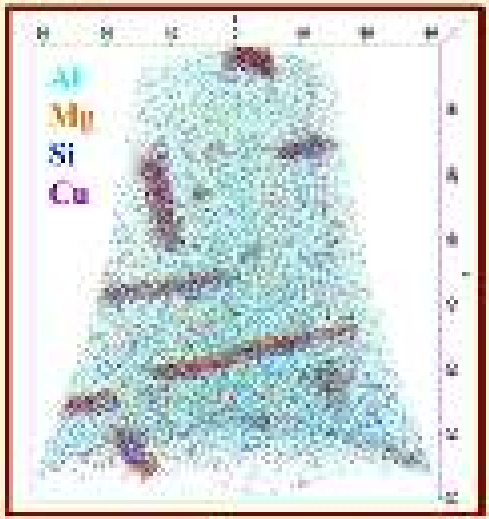

High dose ion irradiation

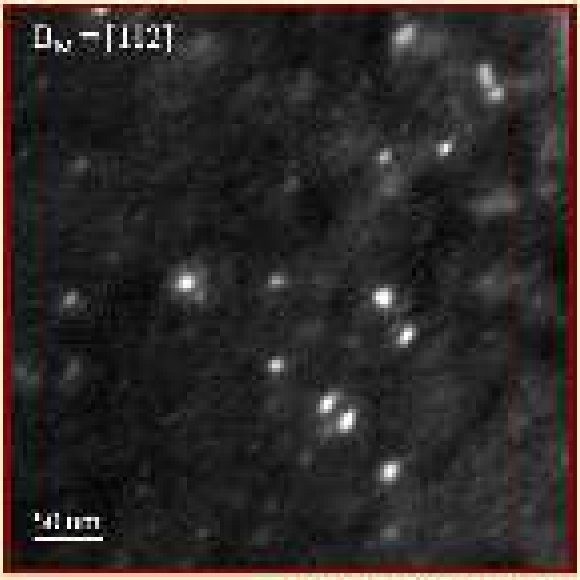

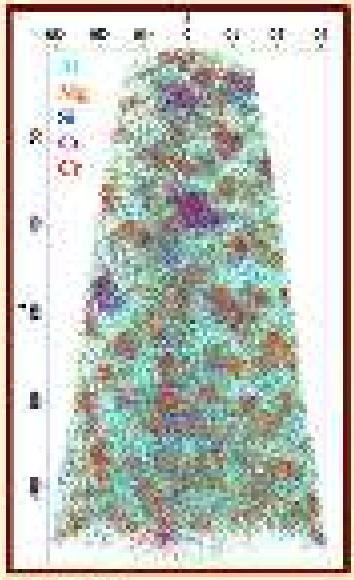

New population of phases